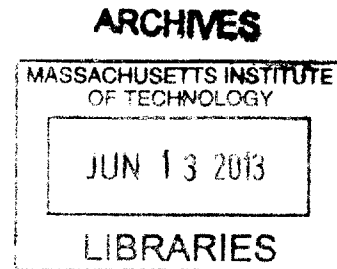# Prediction of Departure from Nucleate Boiling
in PWR Fast Power Transients

by
Giancarlo Lenci

M.S., Energy Engineering
Sapienza University of Rome, 2010

Submitted to the Department of Nuclear Science and Engineering
in partial fulfillment of the Requirements for the Degree of

Master of Science in Nuclear Science and Engineering
at the
Massachusetts Institute of Technology

February 2013

Signature of Author _____
Department of Nuclear Science and Engineering
January 31, 2013

Certified by _____
Professor Kord S. Smith
Professor of the Practice of Nuclear Science and Engineering
Thesis co-Supervisor

Certified by _____
Professor Neil E. Todreas
KEPCO Professor of Nuclear Science and Engineering, Emeritus
Thesis co-Supervisor

Accepted by _____
Professor Mujid S. Kazimi
TEPCO Professor of Nuclear Engineering
Chairman, Department Committee on Graduate Students

Prediction of Departure from Nucleate Boiling
in PWR Fast Power Transients

by

Giancarlo Lenci

ABSTRACT

An assessment is conducted of the differences in predicted results between use of steady state versus transient Departure from Nucleate Boiling (DNB) models, for fast power transients under forced convective heat exchange conditions. Theoretical DNB models based on liquid film thickness variation are adapted and modified from existing studies into a generalized formulation to allow implementation into a reactor simulation code. The formulation is validated using experimental data available at low pressure. An application is performed at Pressurized Water Reactor (PWR) operating conditions, simulating rod ejection accidents.

The transient DNB model is applied to PWR rod ejection accident cases computed by the reactor dynamics code SIMULATE-3K. Rod power profiles deriving from pin power reconstruction are used in a subchannel simulation done with VIPRE to obtain local pin parameters. Results show that a significant delay exists for the occurrence of transient DNB compared to quasi steady-state DNB and in some cases DNB does not occur, even if predicted by quasi steady-state methods.

Most modern codes for PWR thermal hydraulic simulation use quasi steady-state approaches to predict DNB, thus applying a steady-state correlation to time-dependent cases. However, according to the transient DNB model used in this work, a time lag exists between DNB as predicted by steady-state correlations, and effective transient DNB. During that time lag, the liquid film between the wall and the bubbly layer thins until the heated surface is eventually dried out. Such DNB prediction by steady state models is a conservative estimate. This work assesses the consequences of the use of more accurate models for predicting transient DNB, which are desirable to get better knowledge of design margins, to allow optimization of plant safety and efficiency.

Acknowledgements

Table of contents

List of figures

12

13

List of tables

Nomenclature

Acronyms and names

1D	One-dimensional
3D	Three-dimensional
CASMO	Lattice physics multi-group two-dimensional transport code (proprietary code)
CFD	Computational fluid dynamics
CHF	Critical heat flux
CPR	Critical power ratio
CSA	Computer Simulation & Analysis, Inc.
DNB	Departure from nucleate boiling
DNBR	Departure from nucleate boiling ratio
EOC	End of cycle
EPRI	Electric Power Research Institute, Inc.

FTM	Turbulent momentum factor
HI	Hydrodynamic instability
HSN	Heterogeneous spontaneous nucleation
HZP	Hot zero power
IFBA	Integral fuel burnable absorber
LHGR	Linear heat generation rate
LOCA	Loss of coolant accident
LUT	Look-up table
MATLAB	Proprietary code offering a numerical computing environment
MDNBR	Minimum departure from nucleate boiling ratio
MIT	Massachusetts Institute of Technology
MOC	Method of characteristics
MOX	Mixed oxide nuclear fuel
NEA	Nuclear Energy Agency
NRC	United States Nuclear Regulatory Commission
OECD	Organization for Economic Co-operation and Development

PKEs	Point kinetic equations
PWR	Pressurized water reactor
RIA	Reactivity insertion accident
S3K	SIMULATE-3K (proprietary code)
SI	International System of Units
SS	Steady-state
VIPRE	Versatile Internals and Component Program for Reactors (proprietary code)
TH	Thermal Hydraulics
WABA	Wet annular burnable absorber

Symbols

Symbols used in equations throughout all chapters are hereby defined. Their dimensionality is specified first in SI units, as well as when appropriate in other units that appear in this thesis. Vectors are indicated with bold notation, and scalars with regular notation.

Latin characters

A	Area $[\text{m}^2]$
A_β	Turbulent mixing coefficient $[-]$
b	Empirical exponent $[-]$
C	Delayed neutron precursor concentration [same unit as for P]
c	Constant $[-]$
c_p	Specific heat $\left[\frac{\text{J}}{\text{kg K}}\right]$
D	Neutron diffusion coefficient $[\text{m}]$ or $[\text{cm}]$
E	Energy $[\text{J}]$
$F_{\Delta H}$	Enthalpy rise hot channel radial peaking factor $[-]$
F_Q	Point-wise peaking factor $[-]$
G	Mass flux $\left[\frac{\text{kg}}{\text{m}^2\text{s}}\right]$ or $\left[\frac{\text{lb}_\text{m}}{\text{hr ft}^2}\right]$
g	Acceleration due to gravity $\left[\frac{\text{m}}{\text{s}^2}\right]$
h	Heat transfer coefficient $\left[\frac{\text{W}}{\text{m}^2\text{K}}\right]$ or $\left[\frac{\text{MBtu}}{\text{hr ft}^2\,°\text{F}}\right]$
h	Specific enthalpy $\left[\frac{\text{J}}{\text{kg}}\right]$

18

K	Empirical constant or correction parameter [−]
k_{eff}	Reactor eigenvalue, multiplication factor [−]
L	Heated length [m]
l_0	Laplace coefficient [m]
m	Mass [kg]
$\dot{m}$	Mass flow rate $\left[\frac{kg}{s}\right]$ or $\left[\frac{lb_m}{hr}\right]$
n	Empirical exponent [−]
P	Pitch [m]
P	Power [W]
p	Pressure [Pa] or [psi]
$\dot{Q}$	Thermal power [W]
q'	Linear heat generation rate, LHGR $\left[\frac{W}{m}\right]$ or $\left[\frac{kW}{ft}\right]$
q''	Heat flux $\left[\frac{W}{m^2}\right]$ or $\left[\frac{MBtu}{hr\,ft^2}\right]$
r	Position vector [m]
S	Gap width between parallel subchannels [m] or [ft]
T	Temperature [K] or [°C] or [°F]
t	Time [s]
v	Velocity [m/s]
$\dot{w}$	Liquid supply rate $\left[\frac{kg}{s}\right]$
w'	Turbulent crossflow $\left[\frac{kg}{m\,s}\right]$ or $\left[\frac{lb_m}{h\,ft}\right]$

Greek characters

α Correction parameter $[-]$

α Temperature reactivity feedback coefficient $\left[\frac{1}{K}\right]$

α Void fraction $[-]$

β Delayed neutron fraction $[-]$

δ Liquid film thickness $[m]$

η Ratio between transient and steady-state CHF $[-]$

Λ Prompt neutron lifetime $[s]$

λ Radioactive decay constant of delayed neutron precursors $[s^{-1}]$

ν Mean number of neutrons per fission $[-]$

ρ Density $\left[\frac{kg}{m^3}\right]$

ρ Reactivity $[-]$

Σ Macroscopic cross section $[m^{-1}]$ or $[cm^{-1}]$

σ Microscopic cross section $[m^2]$ or $[b = 10^{-24} cm^2]$

σ Surface tension $[Pa \cdot m]$

τ Exponential period of power increase $[s]$

ϕ Scalar neutron flux $\left[\frac{1}{m^2 s}\right]$ or $\left[\frac{1}{cm^2 s}\right]$

χ Fission yield $[-]$

Superscripts and subscripts

General superscripts and subscripts, which apply to different variables, are hereby listed. Self-explanatory subscripts are omitted in this section, while very particular subscripts are defined case-by-case in the text only.

0	Initial
$'$	Per unit length
$''$	Per unit surface
a	Assembly
av	Average
cr	Critical
d	Delayed neutron precursor group
e	Evaporation
F	Flow
f	Saturated liquid
fg	Saturated steam minus saturated liquid, e.g. $h_{fg} = h_g - h_f$
fr	Fuel rods
g	Neutron energy group
g	Saturated steam
hyd	Hydrodynamic instability model

i	Inlet
l	Liquid
nf	Non-fuel
op	Operating conditions
p	Prompt neutrons
ss	Steady-state
t	Total
tth	Thermal thinning model
u	Uncorrected
v	Gaseous phase
w	Wall, i.e. heated surface

1   Introduction

1.1   Overview and motivation

Critical heat flux (CHF) is usually predicted using semi-empirical correlations where sets of data are fit into curves based on theoretical models. Those correlations, which are based on steady-state conditions, can also be applied to time-dependent phenomena, by adopting a quasi-steady-state approach. Such an approach consists of using time-dependent variables together with a steady-state correlation. This produces an error which is often negligible compared to the intrinsic error of the correlation itself. However, in cases where the time evolution of variables is very fast, such as reactivity insertion accidents in pressurized water reactors (PWRs), the time history of parameters becomes more important, and cannot always be neglected.

In this work, an evaluation and assessment is performed of transient critical heat flux prediction methods. Several models are analyzed, compared, and applied to a reference simulation case, i.e. a control rod ejection accident in a PWR. Three models are studied and compared with experimental data:

- Quasi-steady-state approach

- Semi-empirical time-dependent correlation, based on experimental data

- Phenomenological model of the evolution of the liquid film dryout process

Some theoretical models are based on the rate of change of the liquid layer thickness under the bubbly boundary layer on the fuel pin surface. During transients where heat

flux exceeds the critical steady-state value, a finite amount of time is required for the surface liquid layer to evaporate. Therefore, when power excursions are very fast, steady-state CHF correlations tend to provide an incorrect, and conservative prediction of CHF. In this thesis, the error related with the use of steady-state CHF models is quantified for some simulation examples.

1.2 Simulation approach

In modern three-dimensional nuclear reactor core simulation codes such as SIMULATE-3K (S3K), the neutronic model is coupled with a one-dimensional thermal-hydraulic model. The thermal-hydraulic algorithm provides the temperature, coolant density and void fraction parameters needed for updating the nodal cross sections, while the neutronic algorithm provides the heat source distribution. Core-wide simulations are usually done using assembly-averaged radial nodes, or at most 4 radial nodes per assembly. The lack of thermal-hydraulic resolution at pin level does not allow for a local estimation of fuel safety parameters. Such a lack of resolution is acceptable for steady-state cases or slow transients, where separate tools can be used to calculate the peaking factors within the assemblies. However, in the case of locally-initiated fast transients such as rod ejection accidents, higher resolution is needed to estimate the most critical conditions. A subchannel-scale, two-phase, three-dimensional thermal-hydraulic code such as VIPRE can be used to increase the level of thermal-hydraulic detail in the core zones of interest.

In this work, the reactor dynamics code SIMULATE-3K is used to determine the core power distribution and its pin power reconstruction algorithm is used to evaluate the pin power distribution within the hottest assemblies. The power distribution is used as input to VIPRE, which calculates the heat flux, temperature, and mass flux at every axial location for each fuel pin. A transient CHF routine is then used to calculate departure from nucleate boiling (DNB), comparing different prediction models. The results obtained using a quasi-steady state approach for critical heat flux evaluation are

24

compared with other results which take into account transient critical heat flux. The VIPRE simulation offers the advantage of allowing for a subchannel-size radial resolution, while also approximating crossflow between subchannels.

The transients of interest in this work are those which involve a local perturbation, where a significant power difference is produced between pins in the same assembly. This is why the transient chosen for this project is a hot zero power control rod ejection, as described in the OECD/NEA/NRC PWR MOX/UO2 Core Transient Benchmark (Kozlowski and Downar, 2003).

1.3   Thesis outline

This work is organized in the following steps:

- A literature review and analysis of transient DNB prediction methods in flow boiling is performed in Chapter 2. In the same Chapter, a method is identified for the calculation of transient DNB.

- The commercial codes used for PWR transient simulations, i.e. SIMULATE-3K and VIPRE, are described in Chapter 3.

- The simulation procedure is described in Chapter 4. The same Chapter provides a brief description of the transient benchmark upon which the simulations are based, and an example of application of the transient DNB method.

- Results are described and discussed in Chapter 5. The quarter-assembly-averaged non-crossflow results from S3K are compared with the subchannel-resolution results from VIPRE, and with transient CHF results, which take into account the rapid increase in power. The goal is to quantify, for simulation example cases, the error related with the use of quasi steady-state CHF models rather than transient ones.

1.4 Hot zero power rod ejection accidents

PWR rod ejection accident scenarios are caused by the rupture of a control rod drive mechanism casing located on the top of the reactor vessel head, as shown in Figure 1.1. The high pressure difference between the primary system and the containment produces a very fast ejection from the core of the control rods connected to the specific control bank. The insertion of reactivity due to the rod ejection is compensated by *inherent* reactivity feedback mechanisms. The word *inherent* refers to the fact that the occurrence of the feedback is based on unavoidable and totally reliable physical phenomena, e.g. the Doppler broadening of resonances.

In this work, the accident is simulated at hot zero power (HZP) which is a condition, that reactors undergo at startup, of being critical at very low power, while the coolant flows through the primary loop at operating pressure and temperature. HZP is considered as a conservative condition in safety evaluation of rod ejection accidents. This is because at very low power the reactor temperature is not immediately affected by the power level. Due to the negative temperature coefficient of reactivity, a higher power increase is possible than in an ejection from a full power case. Moreover, fully inserted rods introduce a larger reactivity than if they were partially introduced.
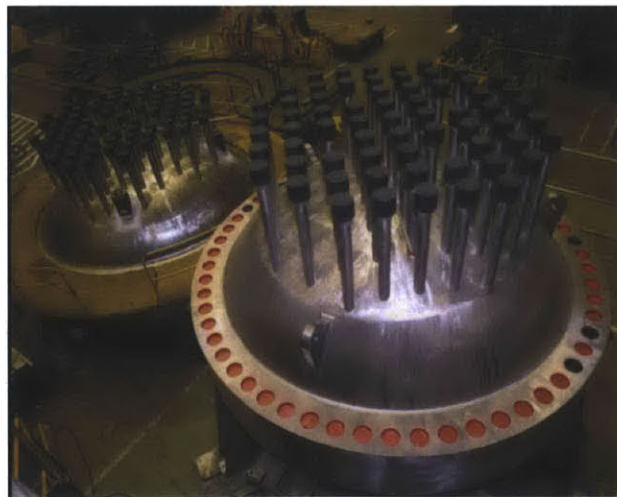
Figure 1.1, PWR reactor vessel heads (source: NRC)

1.5 Prompt feedback reactivity equations

The simplest way to calculate the peak power in a prompt-critical reactor transient is shown in the equations below.

Assuming no external source and constant Λ and β, Point kinetics equations are given by (1.1) and (1.2). If six precursor groups are considered, this creates a system of seven equations.

$$\frac{d}{dt}P(t) = \frac{\rho(t) - \sum_i \beta_i}{\Lambda} P(t) + \sum_i \lambda_i C_i(t) \qquad (1.1)$$

$$\frac{d}{dt}C_i(t) = \frac{\beta_i}{\Lambda} P(t) - \lambda_i C_i(t) \qquad (1.2)$$

The Fuchs-Nordheim model is a simplified point-kinetics method commonly used to understand reactivity pulses in reactors. Since in super prompt-critical reactors the assumption that $\rho \gg \beta$ can be made, delayed neutrons can be neglected, and point kinetics can be approximated as in Eq. (1.3).

$$\frac{d}{dt}P(t) \cong \frac{\rho(t) - \beta}{\Lambda} P(t) \qquad (1.3)$$

A prompt-critical transient is so fast that we can assume that all the heat generated in the fuel remains in the fuel itself, without being transferred to the coolant. This is expressed by Eq. (1.4).

$$T_{fuel} = T_{fuel}^0 + \frac{1}{m\,c_p} \int P(t)dt \qquad (1.4)$$

In Eq. (1.4), $m\,c_p$ represent respectively the mass and specific heat of the fuel. Reactivity variation with temperature is given by the linear expression of Eq. (1.5), assuming a Doppler feedback coefficient independent of temperature. The Fuchs-Nordheim model ignores fuel thermal expansion calculation by simply using the reactivity feedback coefficient α, which can be obtained from empirical data deriving from lattice calculations.

$$\rho(t) = \rho_{rod} - \alpha\left(T_{fuel} - T_{fuel}^0\right) \tag{1.5}$$

Assuming a sudden positive reactivity insertion ρ_{rod}, the temperature at the peak power time can be found by taking the time derivative of Eq. (1.4), and combining it with Eq. (1.3) and (1.5). The result is obtained by setting $dP/dT_{fuel} = 0$, and is given in Eq. (1.6) (Smith, 2012).

$$T_{fuel}^{peak} = \frac{(\rho_{rod} - \beta)}{\alpha} + T_{fuel}^0 \tag{1.6}$$

The temperature of Eq. (1.6) can then be combined with all the other equations to finally obtain the peak power, as in Eq. (1.7).

$$P^{peak} = P_0 + \frac{m\,c_p(\rho_{rod} - \beta)^2}{2\Lambda\alpha} \tag{1.7}$$

2 Transient DNB in flow boiling

2.1 General notions

When heat is transferred from a solid surface to a fluid, the term critical condition refers to a situation in which the heat transfer coefficient suddenly deteriorates. This occurs when the heated surface is no longer in direct contact with a liquid or two-phase layer, but with vapor only. The heat transfer coefficient degradation may produce surface fatigue from thermal cycling, with damaging effects on the heater materials. Prediction of such a phenomenon is very important in the design of industrial heat transfer systems. As an example, non-nuclear industrial applications where the understanding of the critical condition is fundamental are (Sakurai, 2000):

- Cooling systems with high heat flux, such as the interface between the plasma and the wall in fusion reactors.

- Cooling of superconducting magnets by liquid helium, and cooling of high temperature superconductors by liquid nitrogen.

- Cooling of microelectronic systems for advanced computers.

Two separate mechanisms of critical condition can be identified in upward vertical flow boiling. The term departure from nucleate boiling (DNB) generally refers to the critical condition mechanism which occurs at low quality or in subcooled liquid condition. The term dryout refers to critical condition observed at high quality, when the liquid film in contact with the heated surface totally evaporates.

DNB is the critical condition mechanism of major concern in most pressurized water reactor accident scenarios. This thesis focuses only on DNB rather than dryout.

Heat transfer coefficient deterioration caused by DNB leads to a sudden cladding temperature increase that may result into cladding damage. Therefore, safety margins are adopted to prevent such a condition. *Departure from nucleate boiling ratio* (DNBR) is an indicator used to characterize the state of a heat transfer configuration with respect to DNB, as shown in Eq. (2.1) (Todreas and Kazimi, 2011).

$$\text{DNBR} = \left. \frac{q_{cr}''}{q_{op}''} \right|_{\text{for any } z} \tag{2.1}$$

In Eq. (2.1), q_{cr}'' is the critical heat flux, which is the heat flux at DNB, and q_{op}'' is the operating heat flux at the location of interest, z. Usually z refers to an axial location of a given fuel pin. Minimum DNBR, or MDNBR, is the minimum value of DNBR within a specified set of locations (e.g. a fuel pin, a fuel assembly, or the whole core).

2.2 Overview of DNB models

Several theoretical models have been developed to describe the phenomena which lead to DNB. Those models can be divided into three general categories (Todreas and Kazimi, 2011):

- Flooding-like models. The concept behind these models is explained by Zuber (1959, pp. 106-111), as hereby summarized.

  In nucleate boiling regime, bubbles are formed at nucleation sites. If heat flux increases, more bubbles are generated at active nucleation sites, and more nucleation sites become active. If heat flux increases further, the frequency of bubble generation grows until a point when bubbles which follow each other start to touch. At this point some vapor jets are formed. When heat flux increases more, two neighboring jets can interact with each-other, so the liquid boundary layer in contact with the wall is blown off. At this point, a patch of vapor

insulates the heated surface locally. This creates a wall temperature rise which increases the rate of evaporation in other jets. When jets become too dense, they start interfering with each other. The vapor patch grows larger and larger. A characteristic of DNB is that a small increase in heat flux produces a large wall temperature increase. This process is a type of hydrodynamic instability (HI).

- Bubble layer models. According to models in this category, bubbles detached from the wall form a bubble layer which is separated from the wall by a thin film of superheated liquid. The liquid in the thin film evaporates, and it is continuously replaced by a liquid flow from the core of the channel, which moves to the near-wall area by crossing the bubble layer. According to these models, DNB occurs when this compensation is no longer possible.

- Vapor blanket models. According to models in this category, a vapor blanket made of elongated slugs flows close to the liquid film covering the heated wall. DNB occurs when the violent passage of a large vapor slug causes the liquid film nearby to dry out completely.

A different model of DNB proposed by Sakurai (2000) describes a particular phenomenon which, under special flow conditions, causes the critical condition directly at locations of void fraction $\alpha = 0$, without nucleate boiling. Such a direct transition to film boiling is due to explosive-like heterogeneous spontaneous nucleation (HSN). This kind of DNB appears in originally-flooded cavities, independently from the vapor generated from active cavities. According to Sakurai (2000), DNB can be modeled with HSN and HI theories, respectively for higher and lower subcooling.

A perfect theoretical DNB model does not exist, but some models can approximate reality with a small enough relative error, given some sets of assumptions. Most currently-used DNB correlations are based curve fits built using theoretical models and experimental data points.

31

2.3 Theoretical model for transient DNB

The challenge of determining DNB becomes even more complex when time-dependency is added, i.e. when the goal is not only to determine the CHF, but to track its variation with time during fast excursions. A theoretical treatment has been developed by Serizawa (1983). His formulation focuses on the liquid layer underneath the bubbly boundary layer on the heater surface. The rate of change of the liquid layer thickness is the governing parameter which allows prediction of transient DNB.

In steady state, when heat flux is lower than CHF and nucleate boiling occurs, the mass of liquid removed from the liquid film by evaporation is compensated by a continuous supply of liquid from the surrounding medium. This equilibrium causes the evaporation rate $\dot{m}_e$ to be equal to the liquid supply rate $\dot{w}$, as shown in Eq. (2.2).

$$\dot{m}_e = \dot{w} = \frac{q'' A_w}{h_g - h_l} \tag{2.2}$$

In Eq. (2.2), A_w is the heated wall area, and $(h_g - h_l)$ is the enthalpy difference between liquid and saturated steam.

At constant power, the equilibrium given by Eq. (2.2) holds, so the liquid layer thickness δ remains constant. When heat flux increases, the liquid layer thickness is expected to decrease. If the heater power is set at the steady-state maximum heat flux infinitesimally below CHF, indicated by $q''_{cr,ss}$, the equilibrium of Eq. (2.2) is still valid. In this configuration, boiling is stable and the liquid layer thickness is indicated by $\delta_{cr,ss}$. The maximum steady-state heat flux achievable infinitesimally below CHF is the SS CHF, $q''_{cr,ss}$, as formulated by Serizawa (1983) in Eq. (2.3).

$$q''_{cr,ss} A_w = \dot{w}_{cr,ss} (h_g - h_l) \tag{2.3}$$

When evaporation is compensated by liquid supply, DNB is not experienced. On the other hand, if heat flux is raised above CHF, liquid layer evaporation rate becomes

higher than liquid supply rate. In such an unstable condition, the liquid layer becomes thinner and thinner over time, until a point when the wall dries out. During transients where the heat flux exceeds steady-state (SS) CHF, a finite amount of time is required for the surface liquid layer to evaporate. Therefore, when power excursions are very fast, SS correlations prematurely predict the onset of CHF. According to Serizawa (1983), hydrodynamic instability (HI) theories provide a possible criterion to understand the prelude to DNB, and can be used to determine the liquid supply rate to the film at the moment when SS CHF is reached. However, those theories do not describe what happens during the small amount of time prior to DNB, when local phenomena become very important. A qualitative representation of the liquid layer is shown in Figure 2.1.
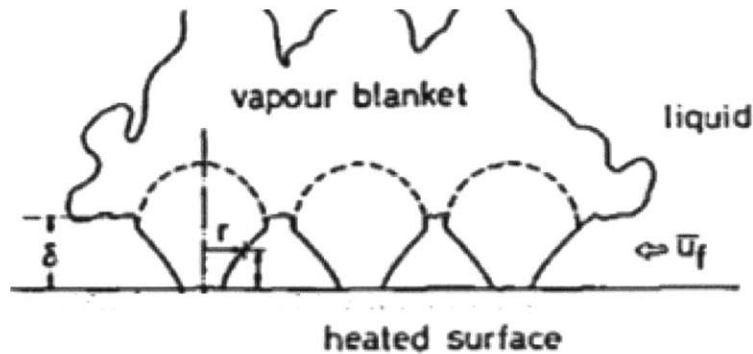
Figure 2.1, Vapor-liquid configuration near DNB (adapted from Serizawa 1983)

Pasamehmetoglu, Nelson and Gunnerson (1990b) proposed a model for transient DNB based on principles from the theoretical study of Serizawa (1983). Two separate phenomena have been identified which lead to transient CHF: hydrodynamic instability and thermal thinning. Both those phenomena are hereby described.

- *Hydrodynamic instability* involves theories which relate film thickness with the Helmholtz critical wavelength produced by shear between liquid and vapor. According to Haramura and Katto (1983), film thickness may be described as in Eq. (2.4), and is inversely proportional to the square of the heat flux.

$$\delta_{hyd} = \frac{1}{q''^2} \cdot \frac{\pi}{2} \sigma \left(\frac{\rho_l + \rho_v}{\rho_l \rho_v} \right) \left(\frac{A_v}{A_w} \right)^2 \left(\rho_v h_{fg} \right)^2 \qquad (2.4)$$

In Eq. (2.4), A_v/A_w is the ratio between the surface covered by vapor stems and the heater area. This ratio was derived by Haramura and Katto (1983) based on a phenomenological CHF model, and on Zuber's (1959) CHF correlation. The resulting expression, which is independent of heat flux, is shown in Eq. (2.5).

$$\frac{A_v}{A_w} = 0.0584 \left(\frac{\rho_v}{\rho_l}\right)^{0.2} \tag{2.5}$$

In future work, it would be desirable to use experiments to check the accuracy of Eq. (2.5), at different pressure ranges. By combining Eq. (2.4) and Eq. (2.5), we can notice that, assuming saturated liquid and vapor, δ_{hyd} is expressed as a function of only heat flux and pressure.

$$\delta_{hyd} = \frac{1}{q''^2_{cr,ss}} \cdot \frac{\pi}{2} \sigma \left(\frac{\rho_f + \rho_g}{\rho_f \rho_g}\right) 0.0584 \left(\frac{\rho_g}{\rho_f}\right)^{0.2} \left(\rho_g h_{fg}\right)^2 \tag{2.6}$$

- *Thermal thinning* is the film thickness reduction due to net evaporation, as described by the time-dependent version of the energy balance of Eq. (2.3), which is shown in Eq (2.7), as adapted[1] from Serizawa (1983).

$$A_w \int_{t_{cr,ss}}^{t_{cr}} q''(t)dt = (A_w - A_v)\rho_l h_{fg}\delta_{tth} + \left(h_g - h_l\right) \int_{t_{cr,ss}}^{t_{cr}} \dot{w}(t)dt \tag{2.7}$$

In Eq (2.7), $t_{cr,ss}$ is the time when the critical condition is reached in steady-state, and t_{cr} is the time when transient CHF is reached. Eq. (2.7) represents an energy balance, where the heat coming from the wall during the transient is equal to the energy required to turn the liquid film into vapor plus the energy required to vaporize the liquid supply water. An implicit assumption in Eq. (2.7) is that $\left(h_g - h_l\right)$ does not vary with time during the transient (Serizawa, 1983).

According to the study of Pasamehmetoglu et al. (1990b), during a power increase transient that leads to DNB, the liquid film thickness follows a hydrodynamic instability model initially, and then switches to a thermal thinning model, as shown in Figure 2.2.

---

[1] The first term in the right hand side of the equation has been modified to take into account that the liquid film only covers only the wetted area $(A_w - A_v)$, instead of the full heated surface A_w. Such a modified term is consistent with Eq. 11 of the paper by Haramura and Katto (1983).
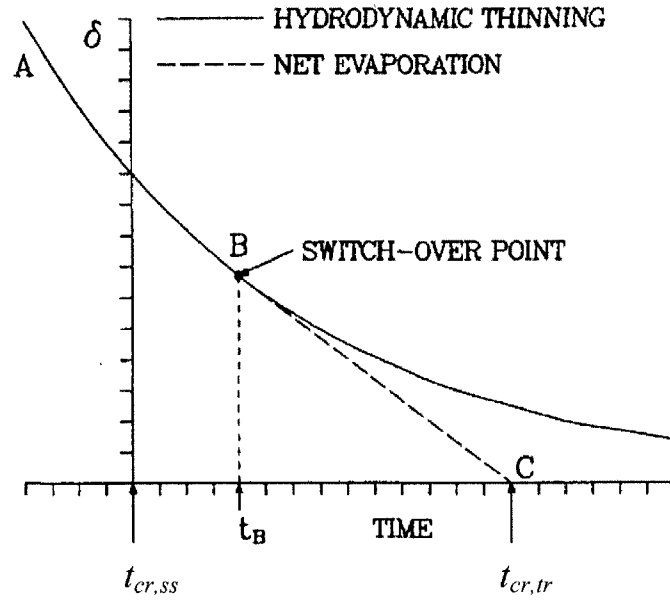
Figure 2.2, Switch-over point between hydrodynamic instability thinning and thermal thinning models for the liquid film (Pasamehmetoglu[2] et al. 1990b)

According to the model of Figure 2.2, HI theories predict the liquid film thickness reduction from the time of steady-state CHF $t_{cr,ss}$ until a switch-over point which occurs at time t_B. Afterwards, thermal thinning models predict the net evaporation of the film, which ends at the transient CHF time $t_{cr,tr}$. After the switch-over point, HI models overestimate the time to CHF. As shown in Figure 2.2, the model which should be used is the one which produces the steepest reduction of the liquid layer film thickness with time. This is expressed by Eq. (2.8), which has been modified[3] from Pasamehmetoglu et al. (1990b).

$$\frac{\mathrm{d}\delta}{\mathrm{d}t} = \min\left(\frac{\mathrm{d}\delta_{hyd}}{\mathrm{d}t}, \frac{\mathrm{d}\delta_{tth}}{\mathrm{d}t}\right) \qquad (2.8)$$

---

[2] The notation has been changed in this figure to obtain consistency with the one used in this thesis: subscript CHF has been replaced with subscript cr.

[3] The relation given by Pasamehmetoglu et al. (1990b) is the following:

$$\left|\frac{\mathrm{d}\delta}{\mathrm{d}t}\right| = \max\left(\left|\frac{\mathrm{d}\delta_{hyd}}{\mathrm{d}t}\right|, \left|\frac{\mathrm{d}\delta_{tth}}{\mathrm{d}t}\right|\right)$$

The same relation has been written in Eq. (2.8) in a version without absolute value brackets, to avoid the risk of errors when one or both of the terms change sign.

The following paragraphs analyze the two terms on the right hand side of Eq. (2.8), leading to a generalized relation for the variation of the liquid layer thickness with time.

Hydrodynamic instability term derivation following Pasamehmetoglu et al. (1990b)

The hydrodynamic instability term of Eq. (2.8) can be found starting from the following relation:

$$\frac{d\delta_{hyd}}{dt} = \frac{\partial \delta_{hyd}}{\partial q''} \frac{dq''}{dt} \tag{2.9}$$

For the sake of simplicity, let us re-write Eq. (2.4) assuming that liquid and vapor phases are at saturation, and condensing all the pressure-dependent terms into a new parameter $f_1(p)$.

$$\delta_{hyd} = \frac{1}{q''^2} \cdot \frac{\pi}{2}\sigma\left(\frac{\rho_f + \rho_g}{\rho_f \rho_g}\right)\left(\frac{A_v}{A_w}\right)^2 (\rho_g h_{fg})^2 = \frac{f_1(p)}{q''^2} \tag{2.10}$$

Where:

$$f_1(p) \equiv \frac{\pi}{2}\sigma\left(\frac{\rho_f + \rho_g}{\rho_f \rho_g}\right)\left(\frac{A_v}{A_w}\right)^2 (\rho_g h_{fg})^2 \tag{2.11}$$

Taking the derivative of (2.10), eq. (2.9) becomes:

$$\frac{d\delta_{hyd}}{dt} = -\frac{2f_1(p)}{q''^3}\frac{dq''}{dt} \tag{2.12}$$

As expected, Eq. (2.12) shows that the time derivative of the hydrodynamic instability liquid layer thickness is negative when power increases over time. This behavior leads to a reduction of the liquid layer during a heat flux increase. Such a reduction is slower for higher heat flux, because of the q''^3 term in the denominator.

Thermal thinning term derivation

An expression for the thermal thinning term can be obtained re-arranging Eq. (2.7) to solve for δ_{tth}. Assuming liquid density at saturation, the result is shown in Eq. (2.13).

$$\delta_{tth} = \frac{1}{\rho_f \Delta h_{fg}\left(1 - \frac{A_v}{A_w}\right)}\int_{t_{cr,ss}}^{t_{cr}} q''(t)\mathrm{d}t - \frac{(h_g - h_l)}{(A_w - A_v)h_{fg}\rho_f}\int_{t_{cr,ss}}^{t_{cr}} \dot{w}(t)\mathrm{d}t \quad (2.13)$$

Eq. (2.13) shows that the thermal thinning model liquid layer thickness at SS CHF is depleted during the transient due to the difference between two counteracting effects: the energy coming from the wall, and the liquid supply. Let us now generalize Eq. (2.13) to find the liquid film thickness due to thermal thinning at any time t between $t_{cr,ss}$ and t_{cr}.

$$\begin{aligned}\delta_{tth}(t) = {} & \frac{1}{\rho_f \Delta h_{fg}\left(1 - \frac{A_v}{A_w}\right)\alpha}\int_{t}^{t_{cr}} q''(\tau)\mathrm{d}\tau \\ & - \frac{(h_g - h_l)}{(A_w - A_v)h_{fg}\rho_f}\int_{t}^{t_{cr}} \dot{w}(\tau)\mathrm{d}\tau\end{aligned} \quad (2.14)$$

Notice that in Eq. (2.16) a correction parameter α has been included, as done by Pasamehmetoglu et al. (1990b), to take into account the effect of subcooling.

$$\alpha = 1 + K\frac{h_f - h_l}{h_{fg}} \quad (2.15)$$

As shown in Eq. (2.15), the correction parameter α depends on an empirical constant K which determines to what extent subcooling is taken into account. Parameter K takes into account the following effects (Pasamehmetoglu et al. 1990a):

- Vapor condensation

- Liquid supply to the film during bubble growth period

- Supply liquid temperature higher than the far-field subcooled temperature

According to Pasamehmetoglu et al. (1990b), we can approximate $K = 1$ at low subcooling. Cases of high subcooling are not simulated in this thesis. The empirical constant K may perhaps be used in future work, supported by experimental data, to take into account HSN effects.

The time derivative of Eq. (2.14) combined with Eq. (2.15) and $K = 1$ yields Eq. (2.16), which is similar[4] to the relation of Pasamehmetoglu et al. (1990b).

$$\frac{d\delta_{tth}}{dt} = \frac{(h_g - h_l)\dot{w}(t)}{h_{fg}\rho_f(A_w - A_v)} - \frac{q''(t)}{\rho_f h_{lg}\left(1 - \frac{A_v}{A_w}\right)} \quad (2.16)$$

Eq. (2.16) shows that the liquid layer thickness due to thermal thinning is increased by a positive term dependent on liquid supply, and decreased by a negative term related with wall heat flux.

The liquid supply rate $\dot{w}$ can be evaluated by analyzing the statistical nature of radial velocity fluctuations at the interface between the liquid and the bubbly layer. The simplified relation of Eq. (2.17) was derived[5] by Pasamehmetoglu et al. (1990b) based on the work of Weidman and Pei (1983).

$$\dot{w}(t) = \left[\frac{q''_{cr,ss}}{q''(t)}\right]^n \dot{w}_{cr,ss} \quad (2.17)$$

---

[4] In the relation of Pasamehmetoglu et al. (1990b) the first term on the right hand side is:

$$\frac{\dot{w}(t)}{\rho_f(A_w - A_v)}$$

This term is equivalent to the one in Eq. (2.16) if the approximation is made that $h_l = h_f$. In reality, it is not necessary to make this approximation since, when Eq. (2.19) is combined to Eq. (2.16), the enthalpy term $(h_g - h_l)$ drops.

[5] Pasamehmetoglu et al. (1990b) use the postulate of Weisman and Pei (1983) that only the radial flow fluctuations higher than the vapor escape velocity v_v can enter the bubbly layer. The probability density function for radial velocity fluctuations is set as a hyperbolic distribution $p(v) = c/v^b$ where c is a probability constant, and b an empirical exponent greater or equal than 2, whose effect is discussed in terms of n in the paragraph after Eq. (2.17). The following equation gives the expected value of v. Notice that in the work of Pasamehmetoglu et al. (1990b) the term $p(v')$ does not appear, probably due to a typo.

$$E(v) = \int_{v_v}^{\infty} p(v')(v' - v_v)dv'$$

From the integration above, the following equation is obtained, where c' is a new constant, and $n = b - 2$.

$$E(v) = c'\left(\frac{1}{v_v}\right)^n$$

From the equation above, Eq. (2.17) can be derived for cases close to the SS CHF condition, considering that the vapor escape velocity v_v is proportional to the wall heat flux, and that the expected value of the radial velocity $E(v)$ is proportional to $\dot{w}$.

Parameter n is an empirical exponent describing the behavior of liquid supply after steady-state CHF. If $n = 1$, the liquid supply is equal to its steady-state CHF value, while if $n = +\infty$ the liquid supply drops to zero beyond CHF. In this work, n is taken equal to 2, as done by Pasamehmetoglu et al. (1990b) based on comparison of the model with the experimental data of Kataoka et al. (1983). Such a comparison is shown qualitatively in Figure 2.3, where η is the ratio between transient and steady-state CHF.
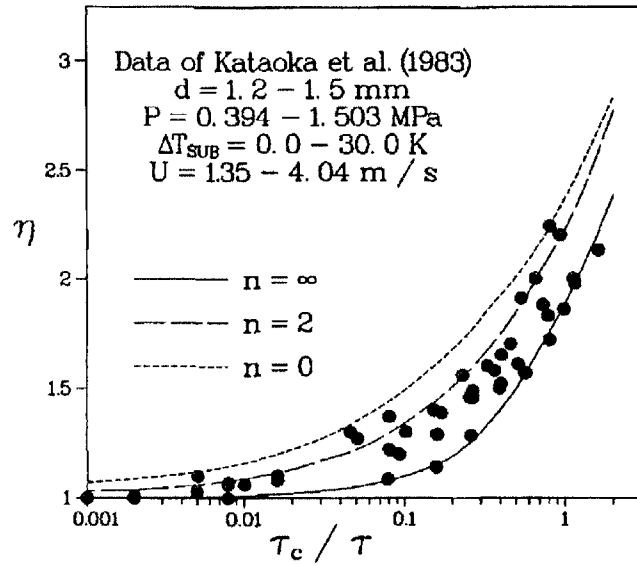
Figure 2.3, Effect of the empirical exponent n (Pasamehmetoglu et al. 1990b)

The critical SS liquid supply rate $\dot{w}_{cr,ss}$ in Eq. (2.17) can be determined by rearranging Eq. (2.3):

$$\dot{w}_{cr,ss} = \frac{q''_{cr,ss}A_w}{\left(h_g - h_l\right)} \tag{2.18}$$

Eq. (2.17) then becomes:

$$\dot{w}(t) = \frac{q''^3_{cr,ss}A_w}{q''^2(t)\left(h_g - h_l\right)} \tag{2.19}$$

Final procedure

Given all the assumptions above, a final relation has been selected for evaluating the transient critical condition. This relation is applicable to power transients where the wall heat flux increases above steady-state CHF, and is more general than the final relation provided by Pasamehmetoglu et al. (1990b), which only applies to exponentially-increasing heat input.

The procedure chosen here to determine transient DNB in a PWR is the following:

- Apply a SS CHF formulation to evaluate the local quasi steady-state DNBR at each axial node of the fuel rod surface. In this work, SS CHF is determined using the 2006 CHF look-up table of Groeneveld et al. (2007).

  At the moment when the quasi steady-state DNBR equals 1 at a given node, evaluate the liquid film thickness at that location by using Eq. (2.6). The film thickness $\delta_{cr,ss}$ in Eq. (2.6) is the starting point from which we can apply the film thickness reduction model described above. One of the assumptions in this model is that the HI film thickness is an instantaneous value which depends only on heat flux and pressure and is independent of the heating history.

- Starting from steady-state CHF at a given location, calculate the liquid layer thickness variation at that location, starting from $\delta_{cr,ss}$, until transient critical condition occurs, i.e. $\delta = 0$, or until steady-state DNBR becomes larger than 1 again. In the latter case, the critical condition does not occur even if predicted by the quasi steady-state model. The liquid layer thickness can be calculated at every time t_{tr} after SS CHF, as in Eq. (2.20).

$$\delta(t_{tr}) = \delta_{cr,ss} + \int_{t_{cr,ss}}^{t_{tr}} \frac{d\delta}{dt} dt \qquad (2.20)$$

The time derivative of δ in Eq. (2.20) is provided by Eq. (2.8).

$$\frac{d\delta}{dt} = \min\left(\frac{d\delta_{hyd}}{dt}, \frac{d\delta_{tth}}{dt}\right) \qquad (2.8)$$

According to Eq. (2.8), the model with the smallest time derivative of δ is applied. During a power transient with liquid layer thickness reduction, the two derivatives are likely both negative. In such a case, the one with the largest absolute value dominates. The approach of Eq. (2.8) is conservative, since it is governed by the model predicting the fastest reduction or the slowest growth of the liquid layer thickness. The time derivative of $d\delta_{hyd}$ is given combining Eq. (2.12) with (2.11) and (2.5):

$$\frac{d\delta_{hyd}}{dt} = -\frac{2f_1(p)}{q''^3}\frac{dq''}{dt}$$

$$= -\frac{\pi\sigma\, h_{fg}^2\rho_g(\rho_f + \rho_g)0.0584^2\left(\frac{\rho_g}{\rho_f}\right)^{0.4}}{\rho_f q''^3}\frac{dq''}{dt} \tag{2.21}$$

The time derivative of $d\delta_{tth}$ is given combining Eq. (2.16) with (2.19) and (2.5):

$$\frac{d\delta_{tth}}{dt} = \frac{(h_g - h_l)\dot{w}(t)}{h_{fg}\rho_f(A_w - A_v)} - \frac{q''(t)}{\rho_f h_{lg}\left(1 - \frac{A_v}{A_w}\right)}$$

$$= \frac{1}{\rho_f\left(1 - 0.0584\left(\frac{\rho_g}{\rho_f}\right)^{0.2}\right)}\left[\frac{q''^3_{cr,ss}}{q''^2(t)h_{fg}} - \frac{q''(t)}{h_{lg}}\right] \tag{2.22}$$

This leads to the following final relation, which is valid both during reduction and growth of the liquid layer thickness, after SS CHF:

$$\frac{d\delta}{dt} = \min\left(\begin{array}{c}-\dfrac{\pi\sigma\, h_{fg}^2\rho_g(\rho_f + \rho_g)0.0584^2\left(\frac{\rho_g}{\rho_f}\right)^{0.4}}{\rho_f q''^3(t)}\dfrac{dq''}{dt}, \\[2em] \dfrac{1}{\rho_f\left(1 - 0.0584\left(\frac{\rho_g}{\rho_f}\right)^{0.2}\right)}\left[\dfrac{q''^3_{cr,ss}}{q''^2(t)h_{fg}} - \dfrac{q''(t)}{h_{lg}}\right]\end{array}\right) \tag{2.23}$$

2.4 Experimental and semi-empirical study

A study by Kataoka, Serizawa and Sakurai (1983) analyzes transient CHF in forced convection boiling. The study uses experiments and theoretical models to build semi-empirical correlations.

The authors collected experimental data of transient critical heat flux for exponentially-increasing heat fluxes. Data have been collected for the following ranges of parameters:

- Exponential period τ between 0.007 s and 10 s, which defines the rate of the heat flux increase over time, as in Eq. (2.24).

$$q''(t) = q_0 \exp\left(\frac{t}{\tau}\right) \tag{2.24}$$

- Pressure between 0.143 MPa and 1.503 MPa

- Inlet subcooling between 10 K and 70 K

- Flow velocity between 1.35 m/s and 4.04 m/s
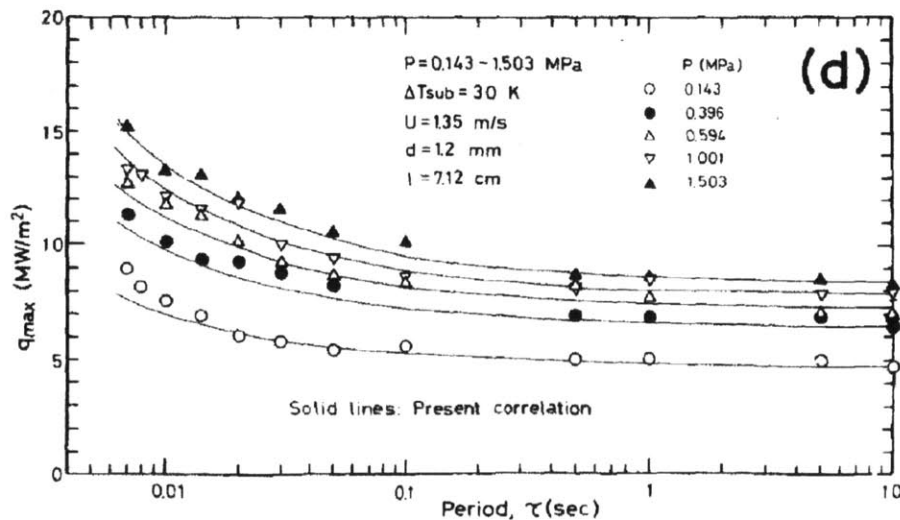
Figure 2.4, Measured data and correlation for transient CHF as a function of the exponential period for different values of pressure (Kataoka et al., 1983)

The authors used a theoretical model to build a relation for transient critical heat flux composed of dimensionless parameters with unknown empirical exponents. The exponents have then been determined by fitting the experimental data.

As an example, Figure 2.5 shows a set of experimental data and correlation lines for different values of water pressure. When building the model, transient heat transfer coefficient correlations have been identified to estimate the wall temperature.

One of the correlations for transient CHF provided by Kataoka, Serizawa, and Sakurai (1983) is given in Eq. (2.25), and according to the authors is applicable to water at pressures ranging from 0.1 to 5 MPa.

$$\frac{q''_{cr,tr} - q''_{cr,ss}}{q''_{cr,ss,00}} = 0.083\ \tau^{-0.63} \tag{2.25}$$

In Eq. (2.25), parameter $q''_{cr,ss,00}$ is the steady-state critical heat flux at zero flow and zero subcooling, i.e. in saturated liquid pool boiling.

The comparison made by Pasamehmetoglu et al. (1990b) between their model and the data measured by Kataoka et al. (1983) resulted in a good agreement, as shown for example in Figure 2.5, where the transient critical heat flux is plotted as a function of the exponential period of the power increase.
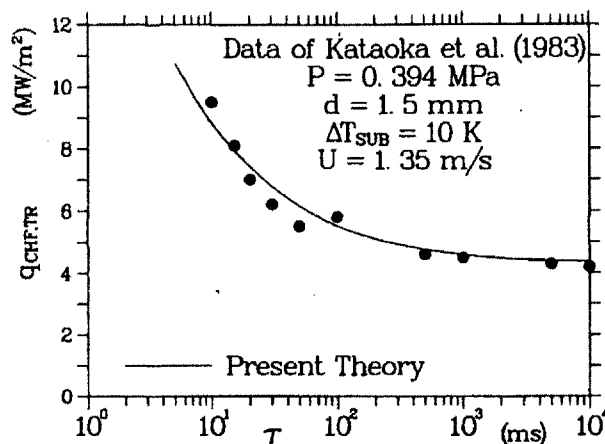
Figure 2.5, Comparison between the model of Pasamehmetoglu et al. (1990b) and the data of Kataoka et al. (1893) (Pasamehmetoglu et al. 1990b)

2.5   Validation of the theoretical approach

Validation of the theoretical approach defined in Eq. (2.23) can be made by comparison with the data points obtained by Kataoka et al. (1983) and with the correlation of Eq. (2.25). For simplicity, in this section the model of Eq. (2.23) is referred to as "theoretical" and the model of Eq. (2.25) as "semi-empirical".

A heated channel where the power increases exponentially with time is simulated using both approaches, and results are compared. For simplicity, we restrict our calculation to a simplified analysis where a heated wall is cooled by water at a given velocity and given far-wall subcooling. The 2006 CHF look-up table (Groeneveld et al, 2007) is used to determine $q''_{cr,ss,00}$, while the assumption is made that an exponential period of 10 s is long enough such that the experimental CHF can be taken as the SS CHF. The comparison has shown a small error between the models, as shown in Figure 2.6 and Figure 2.7.
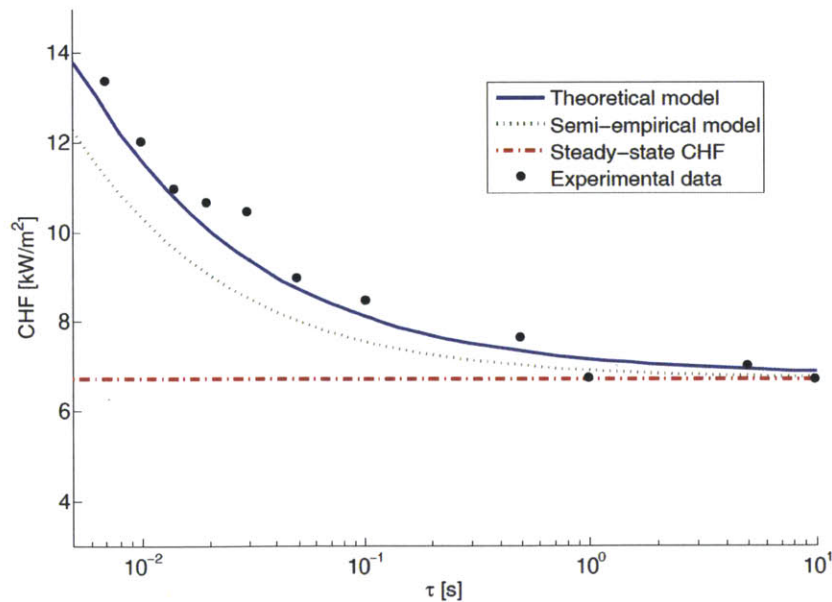
Figure 2.6, Comparison between transient critical heat flux determined with the theoretical and the semi-empirical models, the steady state critical heat flux, and the experimental data from Kataoka et al. (1983), for 10K subcooling, flow velocity of 1.35 m/s, and pressure of 1.503 MPa
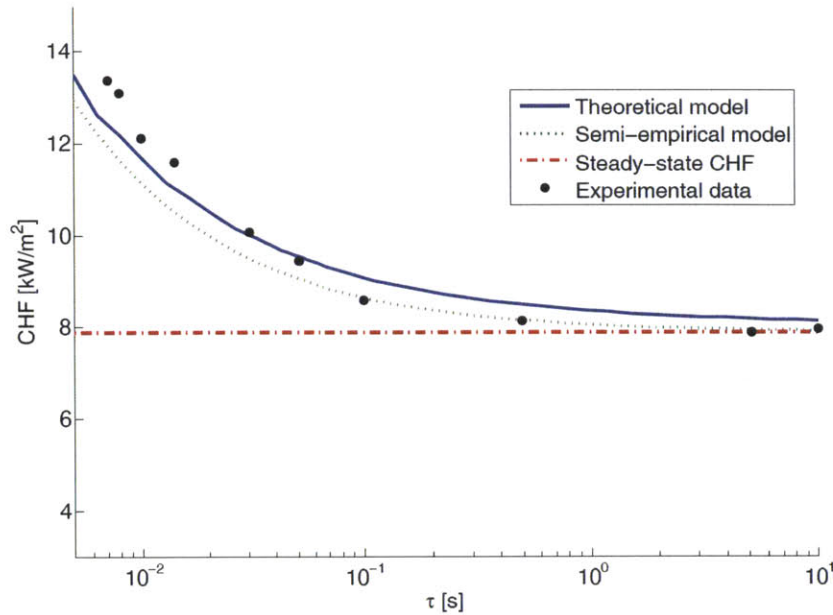
Figure 2.7, Comparison between transient critical heat flux determined with the theoretical and the semi-empirical models, the steady-state critical heat flux, and the experimental data from Kataoka et al. (1983), for 30K subcooling, flow velocity of 1.35 m/s, and pressure of 1.001 MPa

This comparison has been made defining "transient CHF", in a heat transfer configuration with exponentially-increasing heat input, as the heat flux value at the moment of transient CHF, when the liquid layer is depleted. The MATLAB source code used in the routine calculating transient CHF can be found in Appendix C.

2.6 Heterogeneous Spontaneous Nucleation

Experiments in pool boiling (Sakurai, 2000) have shown that Hydrodynamic Instability theories cannot explain some CHF modes which occur at high subcooling. Those events are believed to be caused by explosive-like heterogeneous spontaneous nucleation, HSN. Initially flooded cavities undergo a direct transition from single-phase liquid convection to film boiling, without experiencing nucleate boiling.

Fukuda, Shiotsu and Sakurai (2000) have made some experimental acquisitions in pool boiling, measuring the transient CHF for exponentially increasing power input.

Several correlations have been developed to fit the data points of transient CHF as a function of the exponential period, for different values of pressure and subcooling. However, those correlations are not very applicable to this work, because they have been defined in pool boiling instead of forced convection, and at low pressures of about 400-600 kPa.

It would be desirable to have more data available on the HSN type of CHF, in order to obtain models applicable to the high pressure typical of PWR systems.

3   Simulation codes used

3.1   SIMULATE-3K

SIMULATE-3K is a proprietary code developed by Studsvik Scandpower Inc, which performs transient analysis of the core of commercial pressurized and boiling water reactors. S3K is currently used in nuclear industry for engineering analysis and operator training. The solution method used by the code is time-dependent three-dimensional diffusion theory with six delayed neutron groups, coupled with a thermal-hydraulic channel model. Both those models use the same axial and radial resolution. The radial resolution is of 4 nodes per fuel assembly, while 12 to 25 nodes are typically used in the axial direction to represent the active fuel portion (Grandi, Smith, and Rhodes, 2011). The cross section input to S3K is provided by CASMO, a lattice fuel two-dimensional multi-group transport-based MOC code.

Steady-state solution

Since the diffusion equation is homogeneous, the reactor can be critical at any flux level. The code finds the initial eigenvalue k_{eff} by solving the 3D two-group steady-state diffusion equation.

$$-\nabla \cdot D_g \nabla \phi_g(r) + \Sigma_{tg}(r)\phi_g(r)$$
$$= \sum_{g'=1}^{2} \left[\left(\frac{\chi_g}{k_{eff}} v\Sigma_{fg'}(r) + \Sigma_{gg'}(r) \right) \phi_{g'}(r) \right], g = 1,2 \qquad (3.1)$$

The diffusion equation is solved for homogenized assemblies, and the intranodal flux distribution for both fast and thermal groups is calculated employing a fourth-order polynomial representation.

Transient model

SIMULATE-3K extends the code SIMULATE-3 by adding transient capabilities.

In the transient model some additional terms appear in the diffusion equation, such as the time derivative of the flux, and terms taking into account delayed neutron groups.

$$\frac{1}{v_g(r,t)}\frac{\partial}{\partial t}\phi_g(r,t) - \nabla \cdot D_g(r,t)\nabla\phi_g(r,t) + \Sigma_{tg}(r,t)\phi_g(r,t)$$

$$= \sum_{g'=1}^{2}\left[\left((1-\beta)\chi_g^p\frac{\nu\Sigma_{fg'}}{k_{eff}}(r,t) + \Sigma_{gg'}(r,t)\right)\phi_{g'}(r,t)\right] \qquad (3.2)$$

$$+ \sum_{d=1}^{6}\chi_g^d\lambda_d C_d(r,t) + SE_g(r,t) \ , g = 1,2$$

Parameter $C_d(r,t)$ is taken from Eq. (3.3).

$$\frac{\partial}{\partial t}C_d(r,t) = \beta_d\sum_{g'=1}^{2}\left[\frac{\nu\Sigma_{fg'}}{k_{eff}}(r,t)\phi_{g'}(r,t)\right] - \lambda_d C_d(r,t), \qquad (3.3)$$

$$d = 1,6$$

The code takes into account many complex reactivity effects, among which: fuel burnup, boron concentration, extraneous neutron sources, decay heat sources, fission product concentration (iodine, xenon, promethium, samarium).

Pin power reconstruction

The solution of the 3D diffusion equation by SIMULATE-3K uses spatially homogenized cross sections. This model only captures a smooth variation of the neutron flux within each assembly, without providing information on the detailed pin-by-pin variation of the flux. Such smoothly-varying flux is referred to as homogeneous flux.

48

In order to obtain detailed flux distributions within each assembly, a pin power reconstruction method is used. Such a method assumes that the pin-by-pin flux distribution within every assembly can be approximated as the product of a homogeneous intranodal distribution and a local heterogeneous form function (Rempe, Smith, and Henry, 1989).

$$\phi_g(x,y)_{reactor} = \phi_g(x,y)_{homogeneous} \times \phi_g(x,y)_{form\ function} \quad (3.4)$$

The solution of the fourth-order intra-nodal 3D diffusion equation made by S3K provides some information on the distribution of fluxes within each node (Grandi, Smith, and Rhodes, 2011). Therefore, more information is available than just the flux at every node. This information is used to obtain an approximation of the flux, and therefore power, for every pin and axial location in the whole core.

The main assumption for pin power reconstruction is that the global flux distribution can be considered as spatially separable from the local flux distribution.

The radial flux distribution within every assembly is assumed to be a polynomial obtained by multiplying an x-directed and a y-directed 4th order polynomial. Ignoring cross terms higher than second order, this product leads to 13 unknown coefficients. Those coefficients are evaluated from 13 constraints per group, i.e.:

- 1 node-averaged flux from the general solution

- 4 surface-averaged fluxes from radial node boundaries

- 4 surface-averaged currents from radial node boundaries

- 4 fluxes from corner point interpolation

The following steps are then followed to determine the pin power distribution.

- A "homogeneous" flux distribution is obtained by integrating the product of the fission cross sections and the homogeneous flux distribution.

- Pin power data are interpolated for appropriate local properties (e.g. nodal burnup, coolant density, etc), and CASMO form functions are evaluated.

- A "heterogeneous" flux distribution is evaluated by multiplying CASMO form functions and the homogeneous flux distribution.

As a result, power distribution is predicted for each pin and for each axial node. Pin-by-pin temperature data can be calculated by S3K at the surface of each pin and within the fuel. This calculation is done by using a thermal-hydraulic conduction model which uses the pin power calculated by pin power reconstruction, and the flow parameters based on the thermal-hydraulic model, whose radial resolution is limited to a quarter of a fuel assembly. Due to such a limitation in thermal-hydraulic resolution, fuel temperature is different than the one obtained by calculations which use more radial resolution.

Thermal-hydraulics model

The thermal-hydraulics model of S3K is a combination of a conduction model and a hydraulics model (Grandi, Smith, and Rhodes, 2011). The conduction model calculates the heat flux and temperature distribution in the fuel pins, while the hydraulics model calculates the flow rate, density, and void fraction of water flowing in the channels. Thermal-hydraulic channels have the same mesh as neutronics, i.e. 1 or 4 radial meshes per fuel assembly. Boundary conditions are set for the upper and lower plena: inlet flow and outlet pressure, inlet pressure and outlet flow, or inlet flow and pressure drop.

The thermal-hydraulic model is coupled with the neutronics: at every time step, the neutronics model provides the heat generation rate to the thermal-hydraulics, and receives fuel temperature, water density and void fraction, which are used to evaluate cross section feedback.

S3K contains heat transfer models for several flow regimes: liquid, nucleate boiling, transition boiling, film boiling, transition to single phase vapor, single phase vapor. Several correlations are implemented to define the points of transition between those

flow regimes. A very important transition is the one between nucleate boiling and transition boiling, i.e. the boiling crisis. As mentioned in Chapter 2, DNB occurs at low quality or subcooled conditions, while dryout occurs at high quality, when the liquid film in contact with the heated surface totally evaporates. The models implemented in S3K predict both those critical condition mechanisms.

CHF prediction

The 2006 CHF look-up table of Groeneveld et al. (2007) is used in all cases except for the prediction of low flow and pool boiling conditions. That table provides values of critical heat flux, in kW/m^2, in a three-dimensional array corresponding to different values of pressure, mass flux and quality. The range of the table is shown in Table 3.1. The values in the table which are closer to the center of the ranges of validity are directly derived from experimental data, while the other values are calculated from neighboring experimental data based on selected prediction methods.

Table 3.1, Range of validity of the 2006 CHF look-up table

Mass flux	$0 < G < 8{,}000 \ \mathrm{kg \, m^{-2} \, s^{-1}}$
Pressure	$100 < p < 20{,}000 \ \mathrm{kPa}$
Thermodynamic quality	$x_{CHF} < 1$
Inlet temperature	$T_{in} > 0.01 \ \mathrm{°C}$

Eight different correction factors can be applied to the uncorrected CHF value $q''_{CHF,u}$ to take into account heterogeneities due to fuel bundle configuration, as shown in Eq. (3.5).

$$q''_{CHF} = q''_{CHF,u} \cdot \prod_{i=1}^{8} K_i \qquad (3.5)$$

The correction factors are listed in Appendix A.

3.2 VIPRE01-Mod2.3

VIPRE (Versatile Internals and Component Program for Reactors) is a proprietary system code for nuclear thermal-hydraulic analysis. The code was developed by the United States Electric Power Industry under the sponsorship of EPRI. The code maintenance and development is currently managed by CSA (CSAI, 2012).

VIPRE-01 is based on the subchannel model, and is designed for steady-state and transient analysis, including some severe accidents. The code was developed to calculate core safety parameters such as MDNBR, CPR, maximum fuel and cladding temperature. The code can perform single-phase and two-phase calculations. Conservation of mass, momentum and energy equations are solved using finite-difference methods, assuming incompressible thermally-expandable homogeneous flow, including non-mechanistic models and correlations to take into account two-phase effects such as subcooled boiling and vapor/liquid slip. Moreover, several built-in correlations are available for boiling heat transfer. The code can model fluids different than water if input thermodynamic properties are specified. As a result, the 3D time-dependent field of pressure, velocity, thermal energy and temperature is calculated.

Being a subchannel code, VIPRE-01 models are based on an array of parallel flow channels, where adjacent channels are connected laterally. A modeled channel may represent a subchannel, a water tube, or a larger flow area which lumps together several subchannels or fuel assemblies. In this work, every channel in the model represents a flow subchannel between fuel pins. Heat transfer within walls, hollow tubes, and cylindrical rods is computed through finite-volume conduction, where the properties of the most typical nuclear materials are built-in to the code.

A dynamic gap conductance model can be used to take into account phenomena such as thermal expansion and pressure variation in the fuel-cladding gap. Several input methods are available to assign as an input a time-dependent power map, including power variation tables for each simulation node.

52

4 Simulation description

4.1 The benchmark

Computational benchmarks are a tool to compare the capability of different codes to describe a physical phenomenon. All the reactivity insertion accident (RIA) simulations that have been made in this work are based on the 2003 OECD/NEA/NRC PWR MOX/UO$_2$ core transient benchmark (Kozlowski and Downar, 2003). The benchmark specifications provide the parameters for a full core simulation of a HZP rod ejection in a PWR with a heterogeneous MOX-fueled core.

This benchmark has been chosen because of the following main advantages:

- Specifications are provided for a reference PWR core whose parameters are very similar to those of a commercial PWR of US or European design.

- The simplifications which are defined by the benchmark specifications make the analysis adequate for a manageable comparison between models, and complex enough to allow the observation of most of the phenomena which are important in core design.

- The presence in the fuel of weapons grade MOX assemblies makes the transient particularly challenging, since the delayed neutron fraction is significantly smaller for MOX than for conventional UO$_2$ fuel.

Relevant information from the benchmark specifications is illustrated and described in the following paragraphs.

Main benchmark parameters

The reactor general parameters are listed in Table 4.1, while the parameters related to the individual assemblies are listed in Table 4.2.

Table 4.1, Reactor general parameters (Kozlowski and Downar, 2003)

Parameter	Value
Rated Power, $\dot{Q}_{op}$ [MW$_{th}$]	3565
Coolant inlet pressure [MPa]	15.5
Number of assemblies, n_a	193
Total active core flow, $\dot{m}_{core}$ [kg/s]	15849.4
Active fuel length, L [m]	3.6576
Assembly pitch, P_a [m]	0.2142
Baffle thickness [cm]	2.52
Design enthalpy rise hot channel peaking factor, $F_{\Delta H}$ [-]	1.528
Design point-wise peaking factor, F_Q [-]	2.5
Core loading [t$_{HM}$]	81.6
Target cycle length [GWd/t$_{HM}$]	21.564 (18 months)
Capacity factor (%)	90.0
Target effective full power days [d]	493
Target discharge burnup [GWd/t$_{HM}$]	40.0-50.0
Maximum pin burnup [GWd/t$_{HM}$]	62.0
Shutdown margin [%$\Delta\rho$]	1.3

Table 4.2, Assembly parameters (Kozlowski and Downar, 2003)

Parameter	Value
Fuel lattice	17 × 17
Fuel rods per assembly, n_{fr} [-]	264
Control rod guide tubes per assembly [-]	24
Instrumentation tubes per assembly [-]	1
Non-fuel rods per assembly, n_{nf} [-]	25
Pin pitch [cm]	1.26

54

Pin geometry

The detailed geometry of all pins in the UO_2 and MOX assemblies is illustrated in Appendix B, and corresponds to the assembly maps of Figure 4.1 and Figure 4.2.

Average mass flux

The core-average mass flux is needed as an input parameter in thermal-hydraulic simulations. Its value is not given by the benchmark specifications, but can easily be obtained by dividing the total mass flow rate by the core flow area.

The flow area of each assembly, $A_{F,a}$, can be determined as in Eq. (4.1).

$$
\begin{aligned}
A_{F,a} &= P_a^2 - n_{fr}A_{fr} - n_{nf}A_{nf} \\
&= 0.2142^2 - 264\pi 0.004583^2 \\
&\quad - 25\pi 0.006032^2 \\
&= 0.025604 \text{ m}^2
\end{aligned}
\tag{4.1}
$$

The core-average mass flux is then calculated as in Eq. (4.2).

$$
G = \frac{\dot{m}_{core}}{n_a \times A_{F,a}} = \frac{15849.4}{193 \times 0.025604} = 3207.36 \frac{\text{kg}}{\text{m}^2\text{s}}
\tag{4.2}
$$

Assembly map

Two types of fuel assemblies are loaded in the core. Maps of both types of fuel assemblies are shown in Figure 4.1 and Figure 4.2. The two types are:

- UO_2 assemblies. Those assemblies are composed of normal fuel pins, IFBA fuel pins, and guide tubes/control rod tubes.

- MOX assemblies. Those assemblies are composed of fuel pins with different fissile enrichment, WABA pins, and guide tubes.
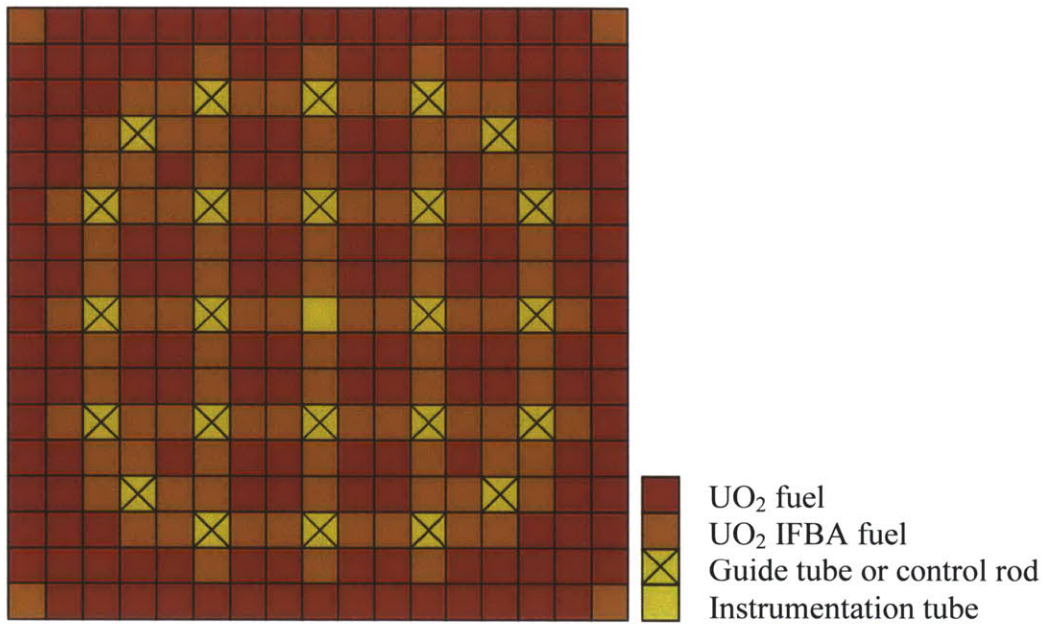
Figure 4.1, UO2 fuel assembly (Kozlowski and Downar, 2003)

UO$_2$ fuel
UO$_2$ IFBA fuel
Guide tube or control rod
Instrumentation tube
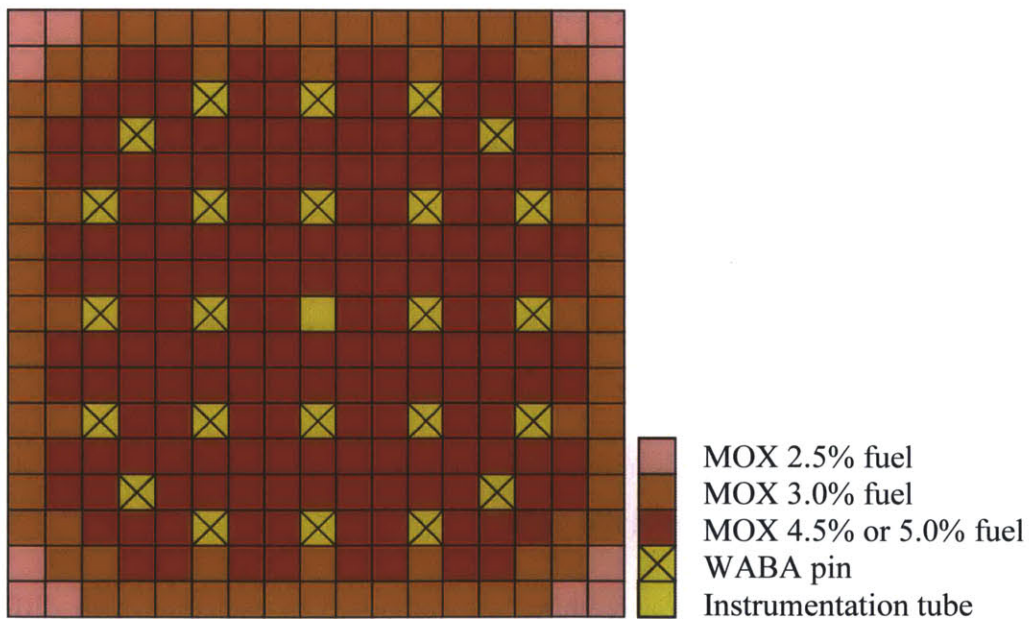
Figure 4.2, MOX fuel assembly (Kozlowski and Downar, 2003)

MOX 2.5% fuel
MOX 3.0% fuel
MOX 4.5% or 5.0% fuel
WABA pin
Instrumentation tube

Core loading configuration

The core loading configuration is provided for one quadrant of the core, since the other three quadrants are symmetric. The assembly where the rod is ejected is located in just one of the four quadrants of the core. The core loading configuration is shown in Figure 5.1.

Transient parameters

Important parameters describing the transient are shown in Table 4.3.

Table 4.3, HZP transient parameters (Kozlowski and Downar, 2003)

Parameter	Value
Initial core power [% of rated power]	10^{-4}
Coolant inlet temperature [K]	560
Coolant inlet pressure [MPa]	15.5
Core average moderator temperature [K]	560

4.2 Calculation procedure

The calculation is made in 4 separate steps, summarized here. More detailed information on the calculation steps is provided in Appendix C, together with the input files or codes of all the routines used.

1. The rod ejection transient is calculated in full core using SIMULATE-3K. In the calculation procedure of the code, the reactor dynamics section is fully coupled with the 1D thermal-hydraulics. The mesh size for both fields is one quarter of a fuel assembly.

2. The pin power reconstruction algorithm of SIMULATE-3K is used to calculate the power of every pin at every axial layer in the assemblies of interest.

3. The transient data for the assemblies of interest is taken directly from S3K pin-wise heat sources. VIPRE performs a transient calculation with pin-channel

resolution, and takes into account cross flows. As a result, a full estimation of VIPRE thermal-hydraulics at every pin axial layer is available.

4. The local parameters obtained from step 3 are used in a MATLAB routine to calculate DNBR using different models. This routine includes quasi-steady-state and transient CHF models.

4.3 Simulation parameters

The simulation parameters and thermal-hydraulic correlations defined in the VIPRE input have been chosen to be the same as those used by S3K. This has been done with the goal of maximizing consistency between the two codes. Table 4.4 shows the results of a comparison of parameters and correlations. The single-phase liquid heat transfer correlation used is described in the following paragraph.

Modified Dittus-Boelter correlation for turbulent flows

The single-phase liquid heat transfer correlation used in both codes is a modified version of the Dittus-Boelter correlation for turbulent flows (Tong and Weisman, 1996), whose expression is given by Eq. (4.3).

$$Nu = C\mathrm{Re}^{0.8}\mathrm{Pr}^{0.4} \tag{4.3}$$

where coefficient C is:

$$C = 0.0333\, E_1 + 0.0127 \tag{4.4}$$

Parameter E_1 is given, assuming an infinite lattice of fuel rods, in Eq. (4.5).

$$E_1 = \frac{A_F}{A_F + A_{rod}} = \frac{P^2 - A_{rod}^2}{P^2} = \frac{0.0126^2 - \pi 0.004583^2}{0.0126^2} \\ = 0.58437 \tag{4.5}$$

58

Table 4.4, Simulation parameters in the two codes

Item	SIMULATE-3K	Vipre	Source
Gap conductance	$h_{gap} = 10^4 \dfrac{W}{m^2 K}$	$h_{gap} = 10^4 \dfrac{W}{m^2 K}$	Benchmark
Theoretical fuel density fraction	100%, since applicable fuel density is already provided by benchmark specifications		-
UO$_2$ thermal conductivity	$k_{UO_2} = 1.05 + \dfrac{2150}{T - 73.15} \dfrac{W}{m \cdot K}$		Benchmark
MOX Thermal conductivity	$k_{MOX} = 0.9\, k_{UO_2}$		Benchmark
Cladding thermal conductivity	$k_{clad} = 7.51 + 2.09 \cdot 10^{-2} T - 1.45 \cdot 10^{-5} T^2 + 7.67 \cdot 10^{-9} T^3 \dfrac{W}{m \cdot K}$		Benchmark
UO2 Specific heat	$c_{p,UO_2} = 162.3 + 0.3038 \cdot T - 2.391 \cdot 10^{-4} T^2 + 6.404 \cdot 10^{-8} T^3 \dfrac{J}{kg \cdot K}$		Benchmark
MOX Spec. heat	$c_{p,MOX} = c_{p,UO_2}$		Benchmark
Radial nodes in fuel pellet	Defined in CASMO input	6 (resonable value)	-
Specific heat cladding	$c_{p,clad} = 252.54 + 0.11474 T \dfrac{J}{kg \cdot K}$		Benchmark
Fraction of power applied in the cladding	-	0.0	Choice
Number of axial meshes	24	24	Reasonable value
Operating pressure	2248.1 psi (15.5 MPa)	2248.1 psi	Benchmark
Inlet coolant temperature	560 K	560 K (548.33 F)	Benchmark
Heat generation in the coolant	2.5%	2.5%	Default of S3K
Power profile in the pellet	Uniform	Uniform	Benchmark
Liquid-only heat transfer correlation	Modified Dittus-Boelter correlation for turbulent flow		Default of S3K
Nucleate boiling correlation	Chen	Chen	Choice

4.4 Methodology for transient DNB calculation

The two main models shown in Chapter 2 for the prediction of transient DNB are the theoretical formulation of Eq. (2.23) and the semi-empirical correlation of Eq. (2.25). Those models have been tested in Section 2.5, and have shown good agreement with the experimental data of Kataoka et al. (1983).

Here we are interested in applying a transient DNB model to the PWR reactivity insertion accident case. The semi-empirical correlation of Eq. (2.25) may not be directly applicable, because it is only valid for pressure up to 5 MPa, while the experimental data of Kataoka et al. (1983) are only available up to a water pressure of 1.503 MPa. No additional semi-empirical correlations or experimental data were found for a pressure of 15.5 MPa. In the present work we assume that the theoretical model of Eq. (2.23), validated in Section 2.5 for lower pressure values, is applicable for higher pressure, of PWR operating conditions. The procedure for transient DNB calculations in the PWR RIA is the following:

1. The VIPRE subchannel calculation is made for the assemblies of interest as described in Section 4.2. In the simulation settings, the film boiling heat transfer is disabled, so the code calculates heat transfer using nucleate boiling correlations even in time steps after steady-state CHF. This is done to make sure that heat transfer parameters are not affected by the heat transfer coefficient degradation due to CHF during the liquid film reduction time (i.e. the time period after SS DNB when transient DNB doesn't actually occur).

2. The following data are collected from the VIPRE output for a selected group of "hot rods" and "hot subchannels" at every time step during the whole transient:

    o Heat flux

    o Cladding outside temperature

    o Mass flux

    o Bulk coolant enthalpy

60

3. The quasi-steady-state critical heat flux is calculated at each node during the whole transient using the 2006 CHF look-up table of Groeneveld et al. (2007), using the correction factors described in Section 3.1, and listed in Appendix A.

4. The quasi-steady state DNBR at every node is calculated using Eq. (2.1).

5. The location and time when the quasi steady-state DNB first occurs is determined from the MDNBR. At that point, the "initial" liquid layer thickness is calculated using Eq. (2.6).

6. The liquid layer thickness variation is calculated by integrating the derivative provided by the theoretical model of Eq. (2.23) over time. In Eq. (2.23), the time derivative of δ is the minimum between the two derivatives determined using the hydrodynamic model and the thermal thinning model. Since a minimum function is used, the most conservative model between the two is always applied, regardless if the liquid layer is being reduced or is growing.

When the liquid layer thickness calculated drops to zero, transient DNB occurs. If the liquid layer thickness does not drop to zero, but starts growing again up to a "stable" thickness, transient DNB does not occur, even if quasi steady-state models predict critical condition.

Example of transient DNB calculation

As an example, the model has been applied to a heat exchange configuration with exponentially-increasing heat flux input, with $\tau = 0.01$, as defined in Eq. (2.24). A fictitious flow boiling heated surface has been modeled with 10 MPa pressure, 1.35 m/s flow velocity, and 2% thermodynamic quality.

The results of this test are shown in Figure 2.1. We may observe from that figure that, while DNB predicted by quasi steady-state methods occurs at time $t = 0.01$ s, transient DNB occurs at time $t = 0.02$ s. The hydrodynamic instability term governs the

liquid layer variation from the point of steady-state DNB until around $t = 0.016$ s, while the thermal thinning term drives the liquid layer thickness variation afterwards.
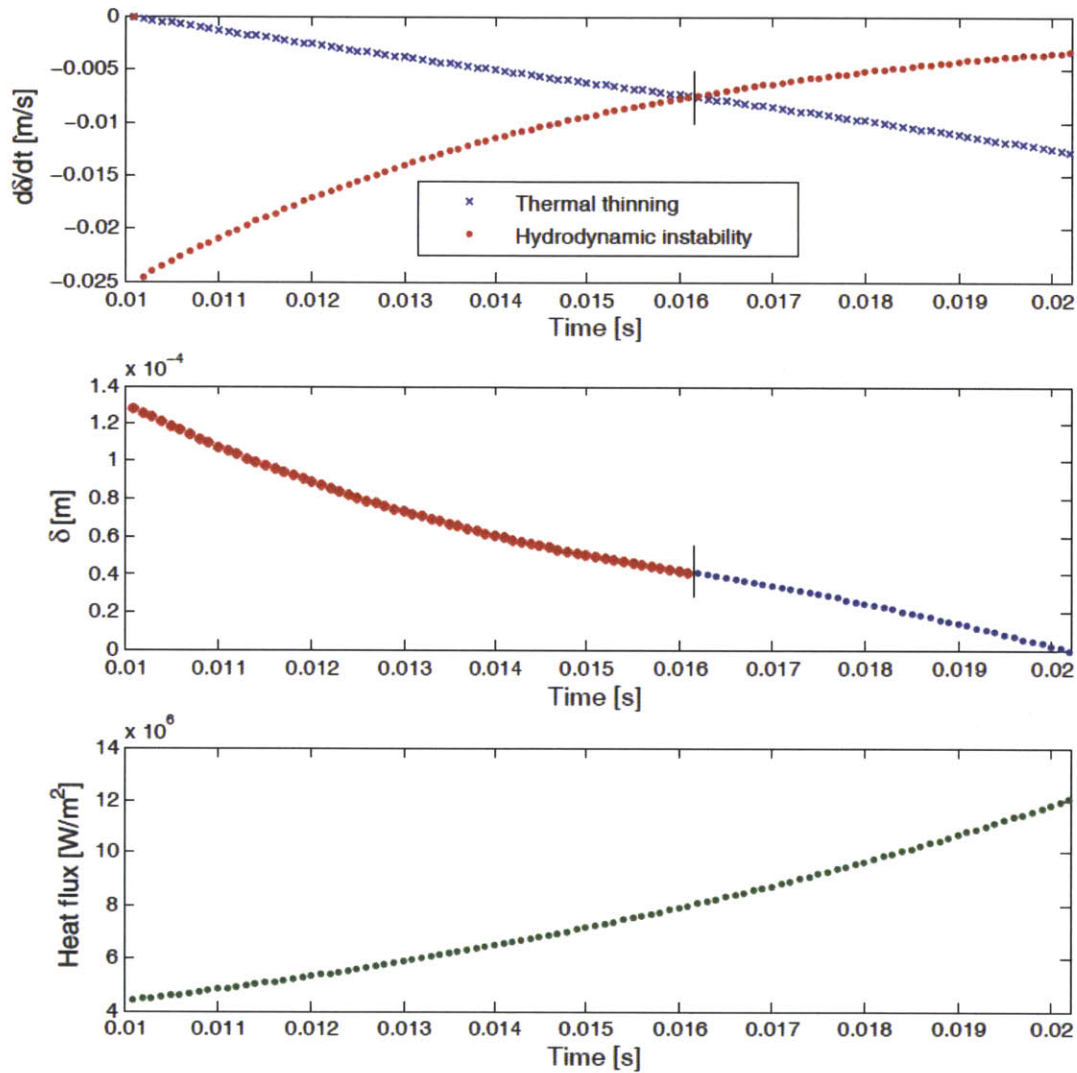
Figure 4.3, Example of application of the model of Eq. (2.23) to a zero-dimensional heat transfer configuration with exponentially-increasing power input

5 Results

5.1 Selection of the assemblies of interest

A map of one quadrant of the core taken from the benchmark specifications (Kozlowski and Downar, 2003) is shown in Figure 5.1. The assembly where the control rod bank is ejected is marked with a circle, in position E5. To avoid the need for useless computational effort, the VIPRE subchannel simulation is not conducted over the whole core, but over a limited number of fuel assemblies of interest. Such a subset of assemblies is selected, with the criterion of including all the locations where the MDNBR can be expected to be during a rod ejection accident.

	1	2	3	4	5	6	7	8
A	U 4.2% (CR-D) 35.0	U 4.2% 0.15	U 4.2% (CR-A) 22.5	U 4.5% 0.15	U 4.5% (CR-SD) 37.5	M 4.3% 17.5	U 4.5% (CR-C) 0.15	U 4.2% 32.5
B	U 4.2% 0.15	U 4.2% 17.5	U 4.5% 32.5	M 4.0% 22.5	U 4.2% 0.15	U 4.2% (CR-SB) 32.5	M 4.0% 0.15	U 4.5% 17.5
C	U 4.2% (CR-A) 22.5	U 4.5% 32.5	U 4.2% (CR-C) 22.5	U 4.2% 0.15	U 4.2% 22.5	M 4.3% 17.5	U 4.5% (CR-B) 0.15	M 4.3% 35.0
D	U 4.5% 0.15	M 4.0% 22.5	U 4.2% 0.15	M 4.0% 37.5	U 4.2% 0.15	U 4.5% (CR-SC) 20.0	M 4.3% 0.15	U 4.5% 20.0
E	U 4.5% (CR-SD) 37.5	U 4.2% 0.15	U 4.2% 22.5	U 4.2% 0.15	U 4.2% (CR-D) 37.5	U 4.5% 0.15	U 4.2% (CR-SA) 17.5	
F	M 4.3% 17.5	U 4.2% (CR-SB) 32.5	M 4.3% 17.5	U 4.5% (CR-SC) 20.0	U 4.5% 0.15	M 4.3% 0.15	U 4.5% 32.5	
G	U 4.5% (CR-C) 0.15	M 4.0% 0.15	U 4.5% (CR-B) 0.15	M 4.3% 0.15	U 4.2% (CR-SA) 17.5	U 4.5% 32.5		
H	U 4.2% 32.5	U 4.5% 17.5	M 4.3% 35.0	U 4.5% 20.0				

Assembly Type
CR Position
Burnup [GWd/t]
Fresh
Once Burn
Twice Burn

CR-A — Control Rod Bank A
CR-B — Control Rod Bank B
CR-C — Control Rod Bank C
CR-D — Control Rod Bank D
CR-SA — Shutdown Rod Bank A
CR-SB — Shutdown Rod Bank B
CR-SC — Shutdown Rod Bank C
CR-SD — Shutdown Rod Bank D
O — Ejected Rod

Figure 5.1, Map of one quadrant of the core (Kozlowski and Downar, 2003)

The pins with the largest power in rod ejection accident scenarios are expected to be very close to the assembly with the ejected control rod bank. Since assembly E5 is twice-burned and surrounded by fresh fuel, the hot rod may be located either in E5, or in some surrounding assemblies with higher reactivity. For example, E4 and D5 are fresh UO_2 assemblies, closer to the core center, with 4.2% initial enrichment; E6 and F5 are fresh UO_2 assemblies with 4.5% initial enrichment; F6 is a fresh MOX assembly with 4.3% initial enrichment.

An analysis has been done to identify the locations where the minimum DNBR can potentially occur. The full-core benchmark transient has been run with S3K, and the assembly-averaged DNBR has been recorded at time $t = 1.5$ s for all the assemblies in the core. The ratio between the DNBR in every assembly and the DNBR in the assembly where the control rod bank is ejected is displayed in Figure 5.2 for the assemblies where that ratio is smaller than 1.5. We notice that the most challenging condition occurs within the 3x3 assembly array around the one from which the rod is ejected. Therefore, work here will focus only on those 9 fuel assemblies.
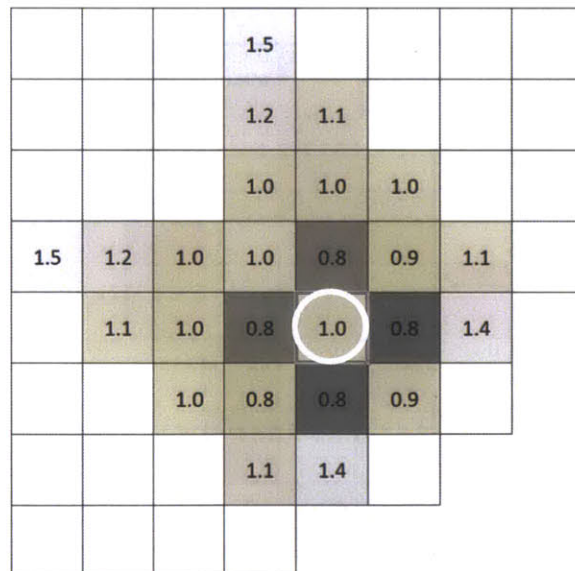
Figure 5.2, Local DNBR relative to the DNBR in the assembly where the rod is ejected, 1.5 seconds after the beginning of the transient (only values lower than 1.5)

5.2 Steady-state test run

As an initial test, a steady-state analysis has been performed with no control rod ejection, with the core critical at 100% rated power. The goal of this run is to test the calculation procedure used for the transient analyses of the following Sections. The steady-state test has been made in time-dependent mode with constant input, in order to use the same time-dependent procedure as in the transient cases.

The S3K pin powers in the selected assemblies are shown in Figure 5.3. Since there is no rod ejection in this case, the hot pin is not necessarily located within the 9 selected assemblies. This is why in Figure 5.3 we observe darker areas towards the upper and left boundaries. The pins in the central assembly have a steady-state power much lower than the average in the plot. This occurs because that assembly has a higher burnup, and fully-inserted control rods.
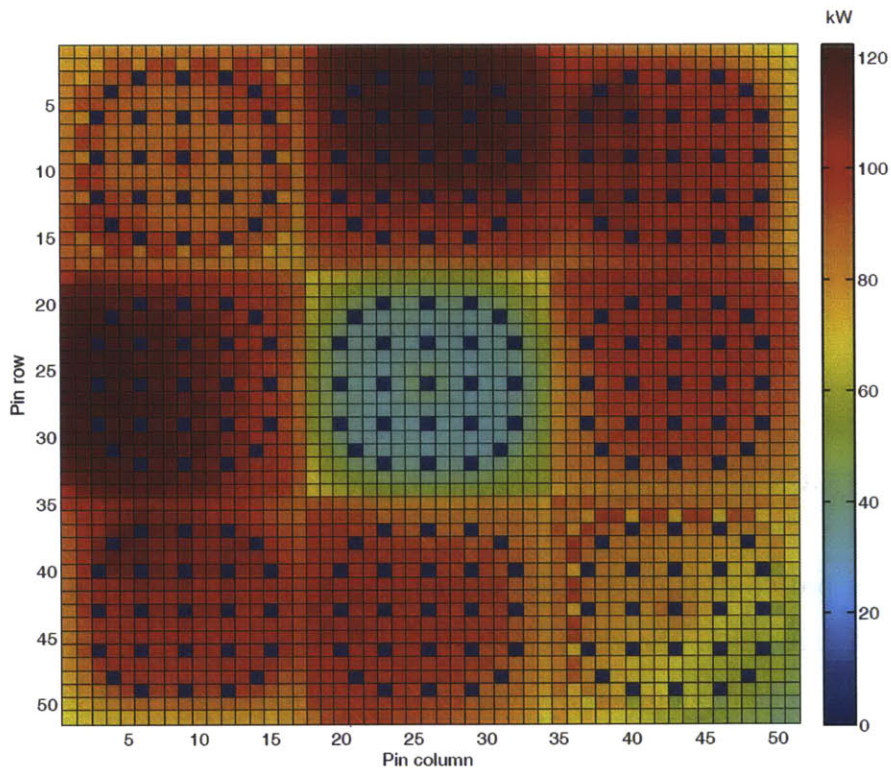
Figure 5.3, Peak pin power in the steady-state test run

65

Symmetrical solution

As we may observe in Figure 5.1, the core has a line of symmetry crossing its center at 45° angle, and crossing through the assembly where the control rod is ejected. This is why results in Figure 5.3 are diagonally symmetric. Given this diagonal symmetry, coordinates describing a fuel pin in maps such as the one in Figure 5.3 are interchangeable, i.e. any result applicable to the fuel pin with coordinates (x,y) is also applicable to pin (y,x). Therefore, from here on, every time we will refer to a pin (a,b), we will equally refer to it or its symmetric pin (b,a).

Power and temperature profile test

A subset of pins has been selected from Figure 5.3. Those pins are marked with letters from A to D, as shown in Figure 5.4.
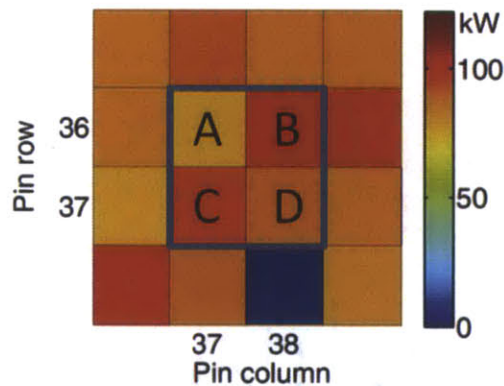
Figure 5.4, Selection of a set of 4 pins in the coordinates of Figure 5.3

The power profile of the two codes for the core midplane axial mesh of pin A has been plotted in Figure 5.5. The values plotted for S3K represent the power generated by the fuel and used as an input to VIPRE, while the values plotted for VIPRE represent the heat transferred through the cladding outer surface divided by $(1 - 0.025)$ to account for the 2.5% direct heat deposition in the coolant. Since this is a steady-state case there is no heat storage effect, so the two lines in Figure 5.5 overlap.

66
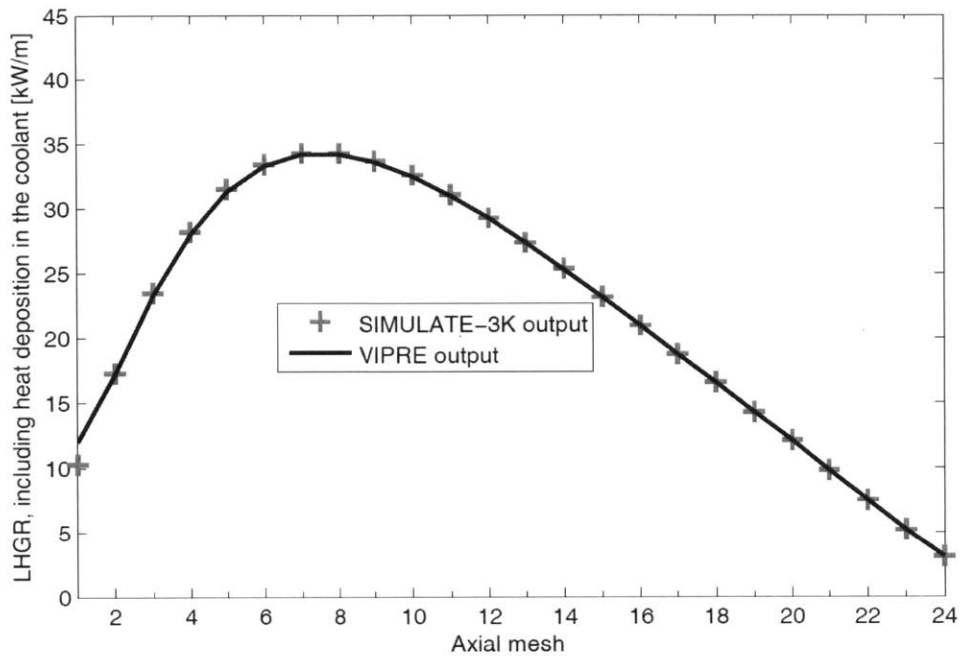
Figure 5.5, Comparison between power outputs of the two codes for pin A, as defined in Figure 5.4, for axial mesh 12/24

The axial variation of the cladding outside temperature for the core midplane axial mesh of pins A to D is plotted in the following 4 figures, and a comparison is made between the S3K and the VIPRE results. In those plots, we observe that the two codes provide similar temperature profiles at the inlet axial meshes, while an offset appears towards the channel outlet, and the VIPRE temperature always higher than S3K.

This temperature difference is explained by the two different ways in which the fluid temperature is computed in the two codes: the S3K model uses a thermal-hydraulic solver where fluid properties are averaged with a radial resolution of a quarter of an assembly, while the VIPRE model uses a local subchannel analysis. This produces a difference between the cladding temperatures calculated in the two codes. An additional cause of differences between the two temperatures is that the VIPRE solution takes into account crossflow, turbulent mixing and spacer effects.
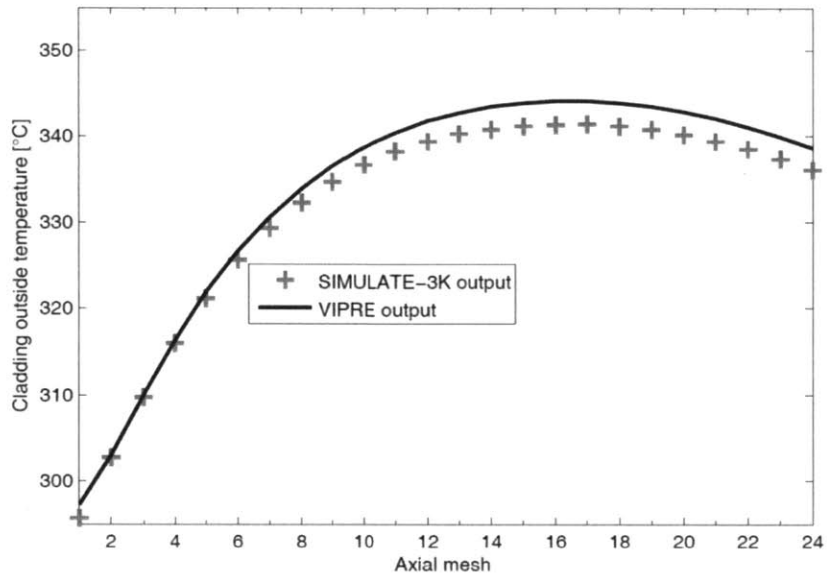
Figure 5.6, Comparison between cladding temperature of the two codes for pin A
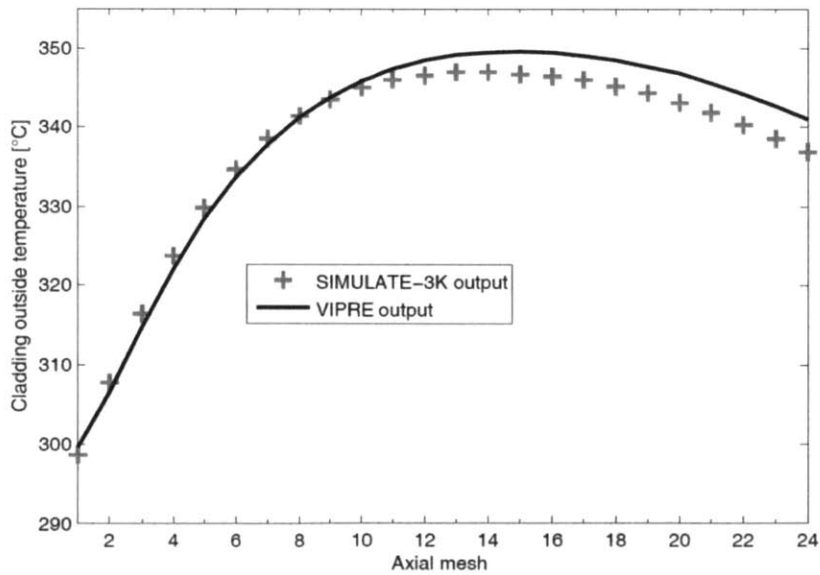
Figure 5.7, Comparison between cladding temperature of the two codes for pin B
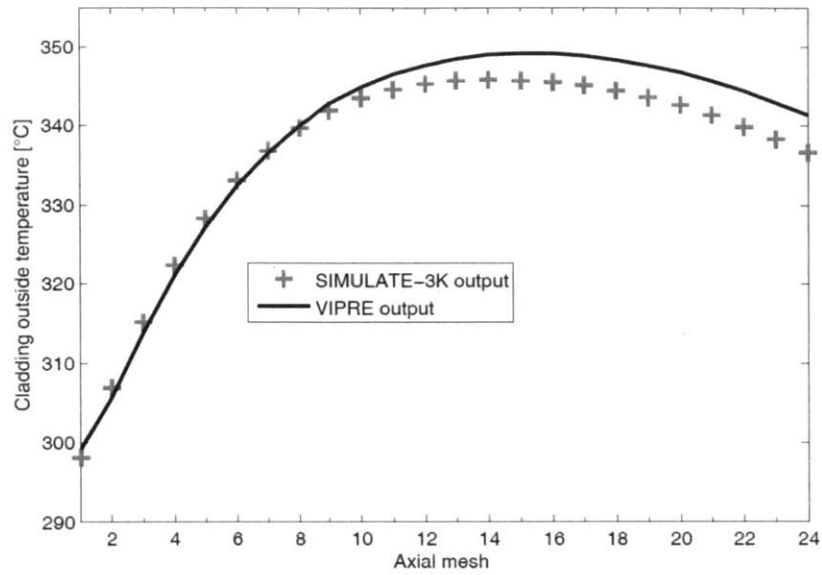
Figure 5.8, Comparison between cladding temperature of the two codes for pin C
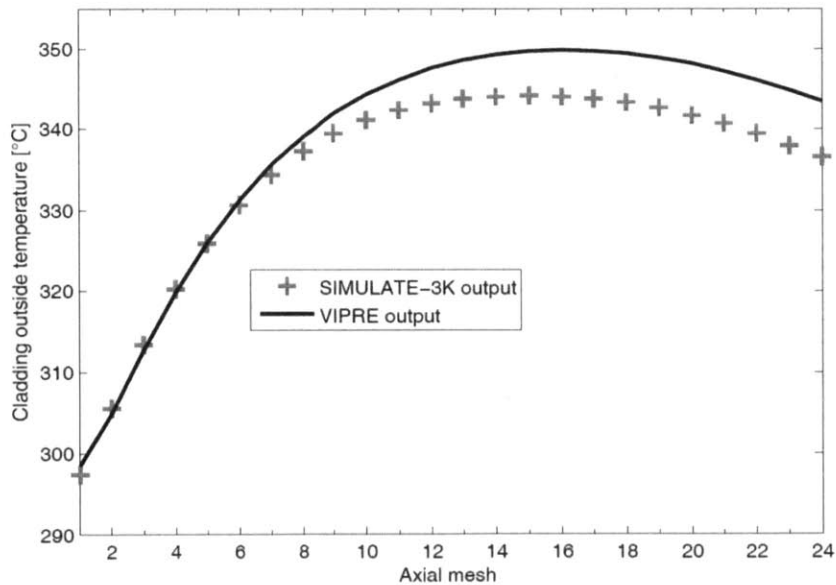
Figure 5.9, Comparison between cladding temperature of the two codes for pin D

5.3 *Transient test: benchmark case*

In this Section results are shown for the standard rod ejection benchmark transient (Kozlowski and Downar, 2003). The purpose of this Section is to test the transient solution procedure. No DNB calculations are made, since this transient does not get close to DNB. Higher power transients are simulated in the following Sections.

Reactivity and power variation

The reactivity and power variation during the transient as calculated by S3K are shown in Figure 5.10. The reactor is super prompt-critical for an amount of time shorter than 0.5 seconds, and reaches a peak power of more than 120% the rated value.
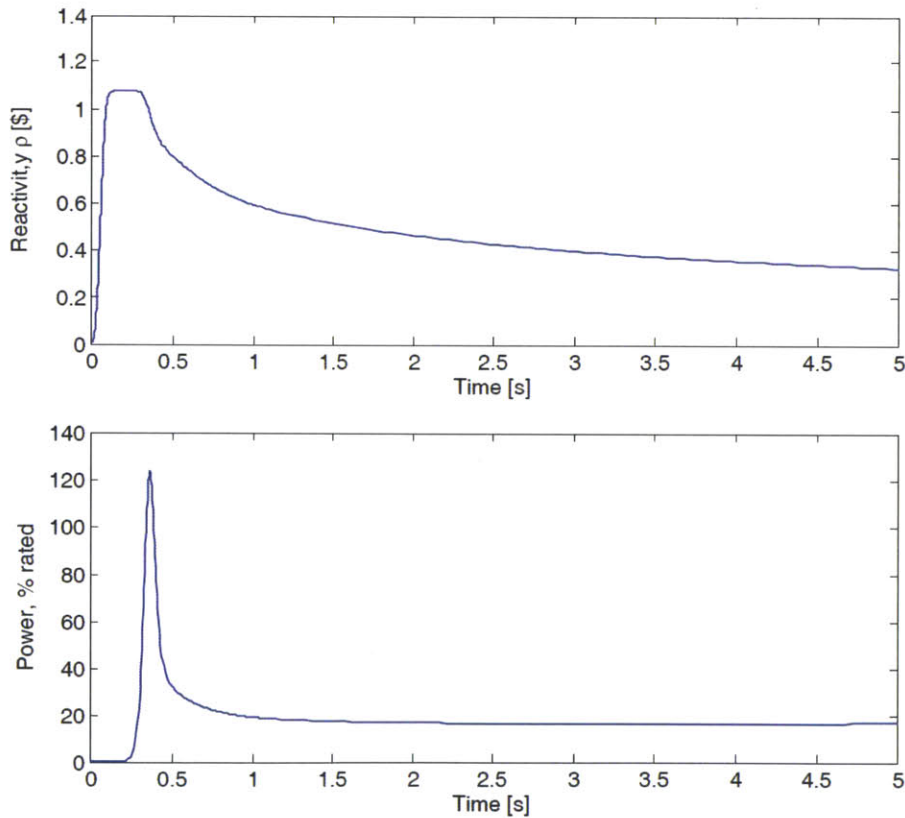
Figure 5.10, Reactivity and power variation during the benchmark transient

Hot rod search

The areas where the hot rod is expected to be can be found by analyzing the pin power variation with time as provided by the S3K calculation. The peak power reached by every pin has been plotted for the area of interest in Figure 5.11, where we observe that the rod with the highest power is (36,38), while another hot area is located right below the central assembly.

In the same figure, we observe that the central assembly is not the one where the highest power values are recorded. Numbering those assemblies from 1 to 9 (starting from the top row, from the left to the right), assemblies 4,8,9 and their symmetric ones all have fresh fuel, as shown in Figure 5.1. This is why they have a higher power than assembly 5. Notice that the pins with highest power in those assemblies are all located on the side facing the central assembly.
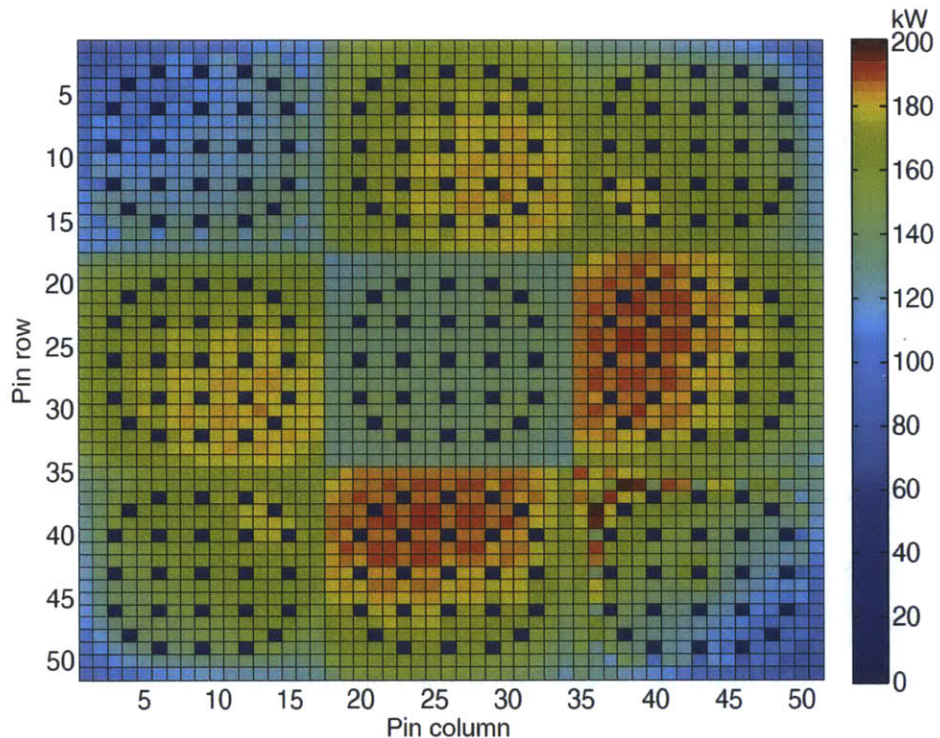
Figure 5.11, Peak pin power

The same hot locations plotted in Figure 5.11 can be observed in Figure 5.12, which shows the energy deposited in the fuel pins from the beginning of the transient until the end of prompt-criticality, which occurs around $t = 0.35$ s.

By comparing Figure 5.11 and Figure 5.12 we observe good correspondence between pins with highest peak power and the pins where the highest energy is deposited.
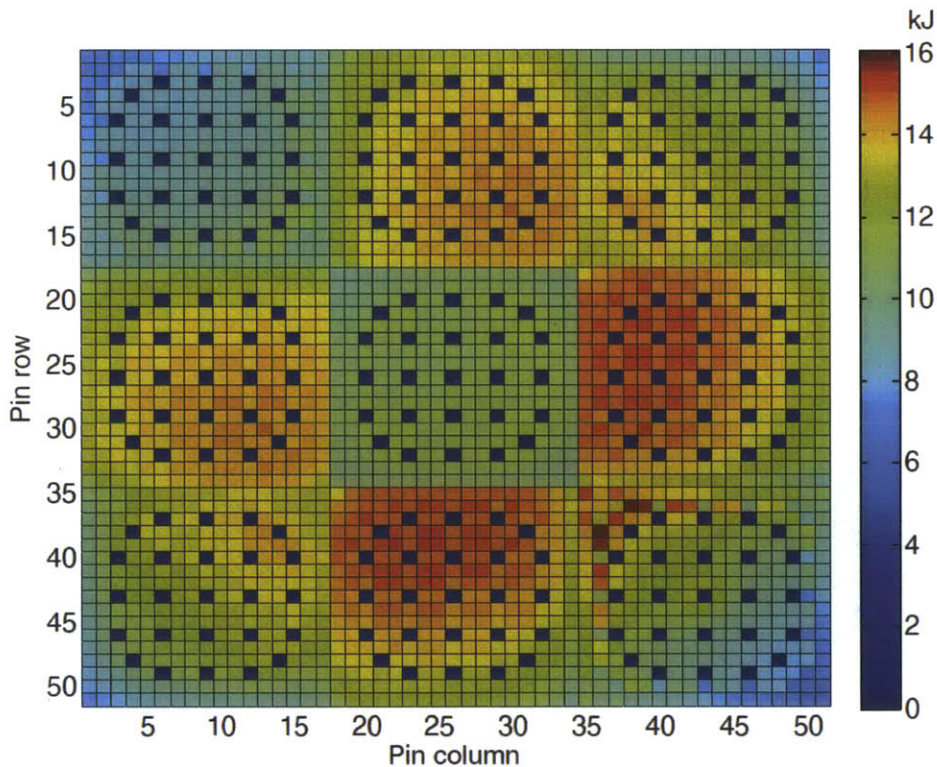
Figure 5.12, Energy deposited before the end of prompt-criticality

S3K results provide core-wide MDNBR values all higher than 7 during the transient. Since in this work we are interested in DNB, in the following tests we will increase the rod worth, to bring the core to critical condition.

Before proceeding to the DNB test, let us plot some results for the hot pin of the benchmark case, which is in position (36,38).

Hot rod cladding outside temperature

The cladding outside temperature is calculated by S3K using the pin conduction model, and by VIPRE. As shown in Figure 5.13, good agreement is obtained at the core midplane axial mesh between the two codes.
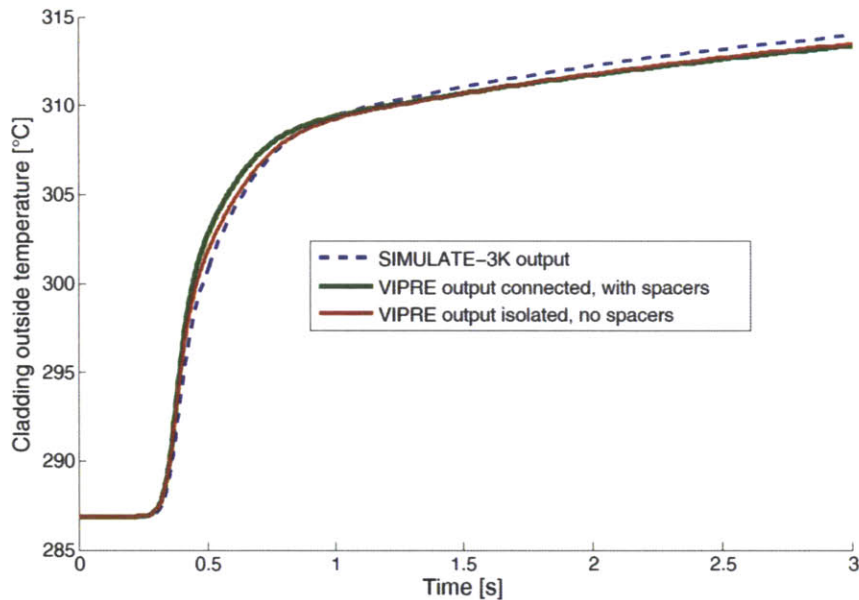
Figure 5.13, Cladding outside temperature, hot rod (36,38), axial mesh 12/24

Two VIPRE results are plotted in Figure 5.13: one calculated with crossflow between pins, including the modeling of spacer grids and turbulent mixing, and the other one assuming isolated subchannels with no spacer grids. For simplicity, the former results are referred to as "connected", and the latter as "isolated". As expected, isolated results are more similar to the S3K solution than the connected ones, although the difference is not pronounced. Connected temperature results are a bit higher than isolated ones during the fast temperature increase. This because a combination of crossflow between adjacent subchannels, turbulent mixing, and spacer grids produces a lower heat transfer coefficient, as shown in Figure 5.14. Figure 5.15 shows that the axial profile of the cladding outside temperature is larger for the VIPRE solution than for the S3K solution in the higher axial meshes, as observed also in the steady-state case. This effect is probably due to the fact that S3K uses water parameters which are averaged

with a radial resolution of a quarter of an assembly, while VIPRE uses a subchannel radial resolution. This results in the lower S3K cladding outside temperature at high axial meshes shown in Figure 5.16.
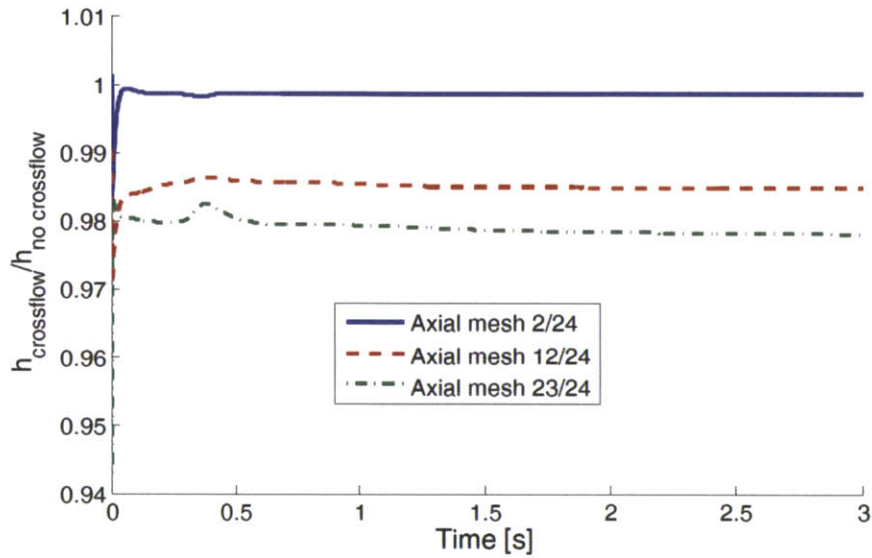
Figure 5.14, Comparison between VIPRE heat transfer coefficient with and without crossflow, turbulent mixing, and spacer grids
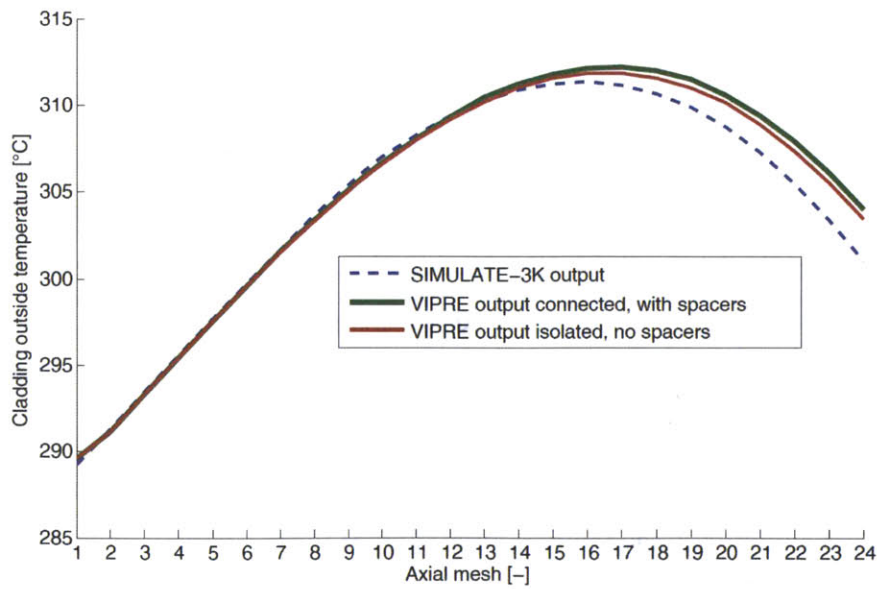
Figure 5.15, Cladding axial temperature profile at time 1s, for the hot rod (36,38)
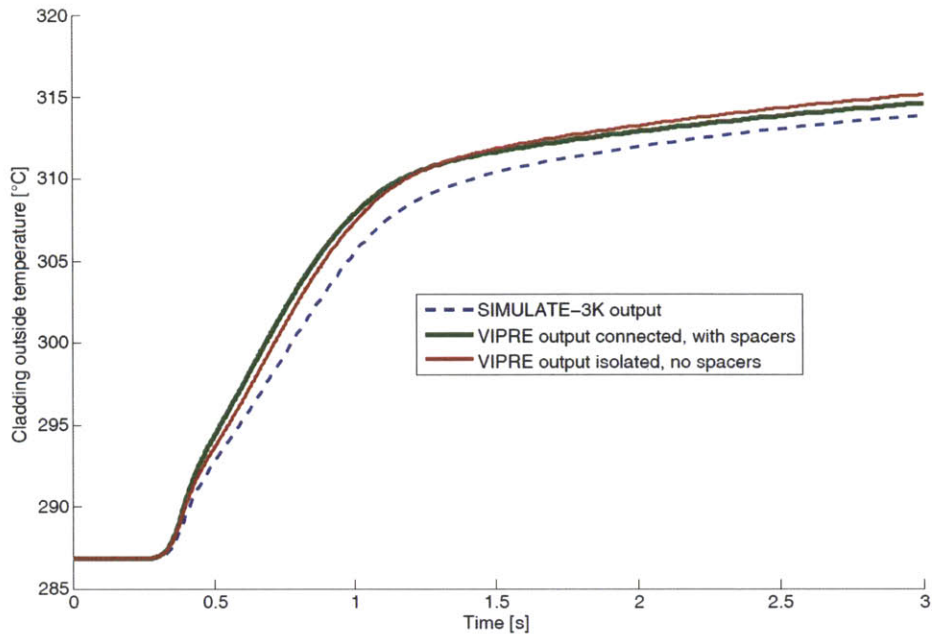
Figure 5.16, Cladding outside temperature, hot rod (36,38), axial mesh 22/24
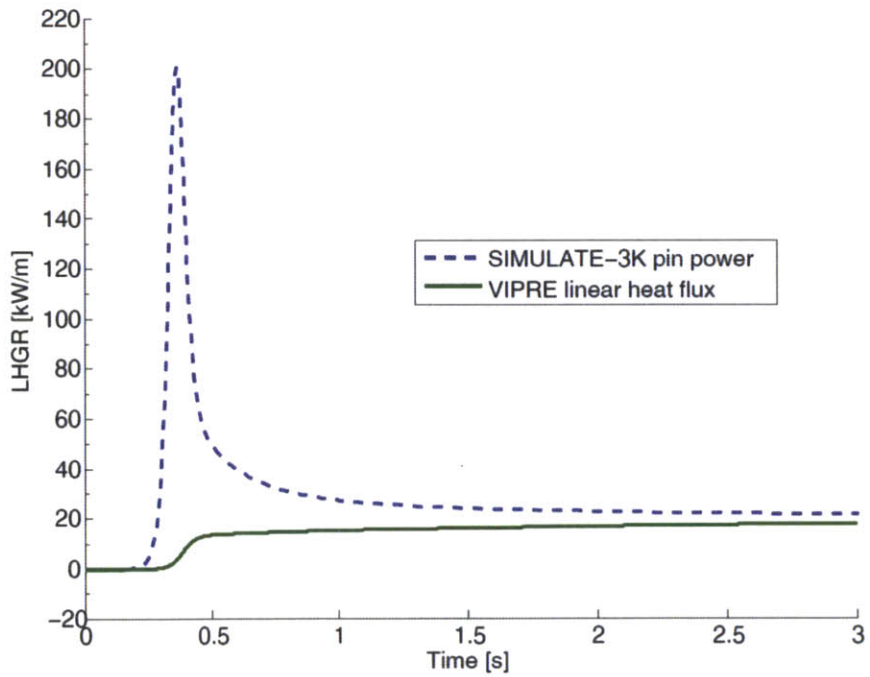
Figure 5.17, LHGR for the hot rod, at axial mesh 12/24

The effect of crossflow, spacer grids, and turbulent mixing on the VIPRE results can be analyzed by looking at Figure 5.18. In that figure, several solutions with crossflow are compared with the isolated case, to identify the effect of spacers and turbulent mixing.

We may notice that solutions without turbulent mixing are closer to the isolated case during the whole transient, while solutions with turbulent mixing undergo a temperature excursion of about 1 K with respect to the isolated case around time $t = 0.5$ s, when the cladding undergoes a fast temperature increase. Such an effect disappears over time, towards the end of the transient, as all variables get steadier. It may be interesting to analyze such an effect in future work, and to compare this result with more complex turbulence models, even using computational fluid dynamics (CFD).

We can also notice that spacers always produce a small cladding temperature reduction, probably because mixing is enhanced.
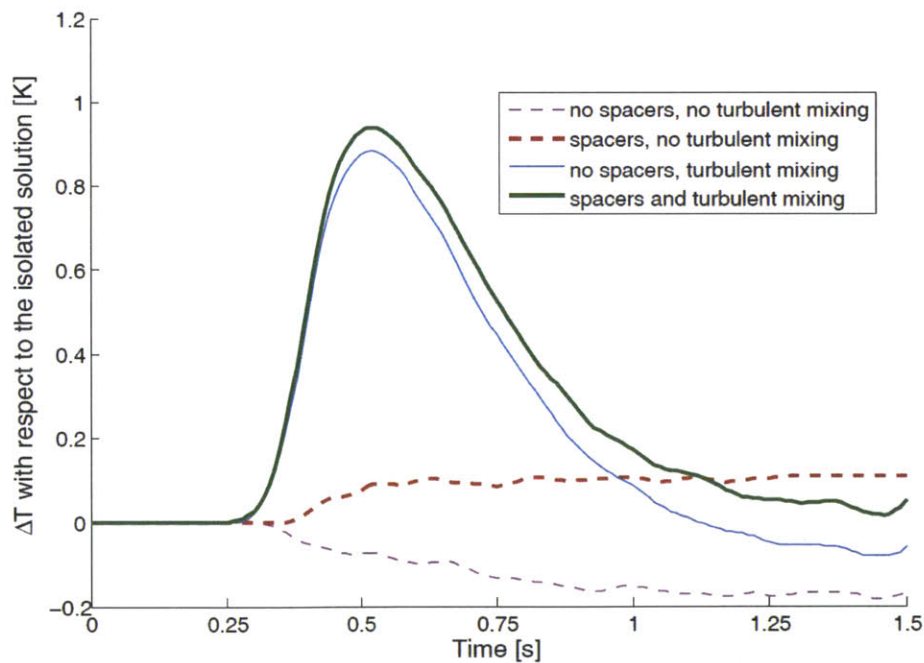
Figure 5.18, Effect of spacer grids and turbulent mixing on the VIPRE solution. Temperature difference with respect to the isolated solution calculated at the hot rod axial mesh 12/24

Hot rod power and energy

The power generated during the transient is plotted in Figure 5.17 for the midplane axial mesh of the hot rod. We observe that a large power excursion occurs for the pin power in S3K, while the VIPRE heat flux variation is much smoother. The difference between the areas underneath the two curves is the energy stored in the fuel pin.

The integrals over time of the power curves of Figure 5.17 are shown in Figure 5.19. Figure 5.19 shows that at the end of the transient, the energy generated in the fuel is 85.73 kJ/m and the energy transferred to the coolant through the cladding is 42.2 kJ/m. The difference between those two values is given by the following subtraction, where the 2.5% coolant heat deposition is appropriately taken into account.

$$\Delta E' = 85.73(1 - 0.025) - 42.2 = 41.4 \text{ kJ/m} \qquad (5.1)$$
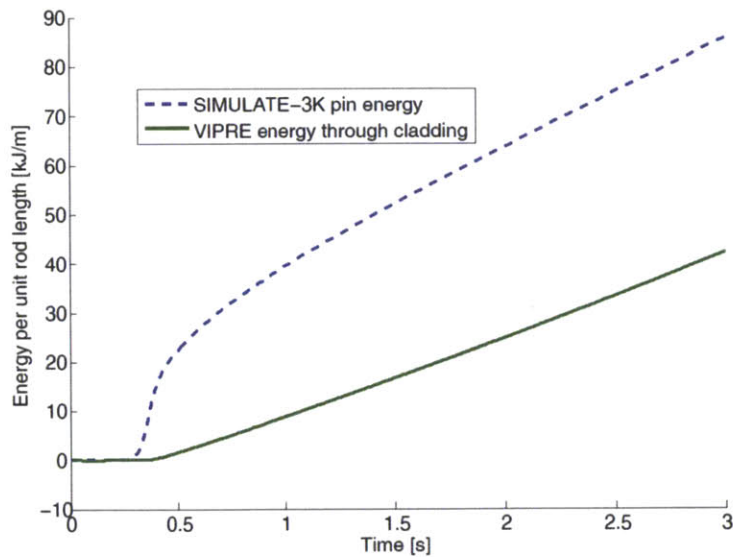
Figure 5.19, Energy generated by the pin and energy flowing through the cladding, per unit length, for the hot rod, at axial mesh 12/24

According to the VIPRE results, the average fuel temperature at the beginning and at the end of the transient is respectively 287 °C, and 576 °C. This translates into a temperature difference of 289 °C. The integral average of fuel specific heat of the fuel

between 287 °C and 576 °C can be determined from the relation shown in Table 4.4, and is equal to 0.279 kJ/kg. We can use all the values above to calculate the temperature increase that would be derived from the deposition in the fuel of 41.4 kJ/m:

$$\Delta T = \frac{\Delta E'}{\rho A c_p} = \frac{41.4 \frac{\text{kJ}}{\text{m}}}{10240 \frac{\text{kg}}{\text{m}^3} \times \pi (0.003951 \text{ m})^2 \times 0.279 \frac{\text{kJ}}{\text{kg K}}} = 321 \text{ °C} \qquad (5.2)$$

The value found in Eq. (5.2) is higher than 289 °C, but close enough to justify the order of magnitude of the energy difference in Figure 5.19. A slightly smaller and more accurate temperature value than the one in Eq. (5.2) would be obtained if the sensible heat deposited into the cladding and the heat transferred axially through the fuel rod were taken into account. Finally, fuel enthalpy is plotted in Figure 5.20, as calculated by the two codes for the hot rod and core midplane. We may notice that the value calculated by S3K is higher than the one of VIPRE. This is probably a result of the higher coolant temperature calculated by S3K at the core midplane axial mesh, as shown in Figure 5.13. In fact, a higher cladding outside temperature translates into a higher fuel temperature, so more sensible heat is accumulated in the fuel.
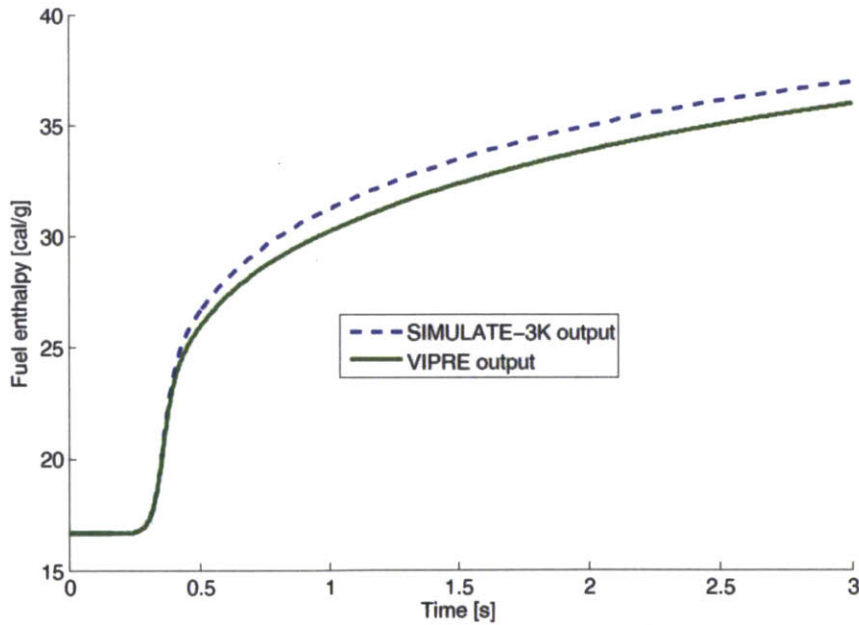
Figure 5.20, Hot rod fuel enthalpy at axial mesh 12/24

5.4 Transient with 155% rod worth, ejection in 1 s

A rod ejection case has been run with 155% rod worth with respect to the benchmark specifications, and with a rod ejection time of 1 s. This configuration has been chosen in order to bring the fuel rods to the critical heat flux condition, so that the transient DNB model could be applied.

Reactivity and power variation during this transient are plotted in Figure 5.21. In those two plots, we can notice a damped oscillation of reactivity over time. Such a behavior is justified by theoretical considerations: a positive reactivity insertion, taking into account delayed neutrons, leads to a damped reactivity oscillation. Reactivity variations are also due to the fact that the control rod moves until time $t = 1s$. The variation of core power with time shows that a peak is reached at about 25 times the rated power.
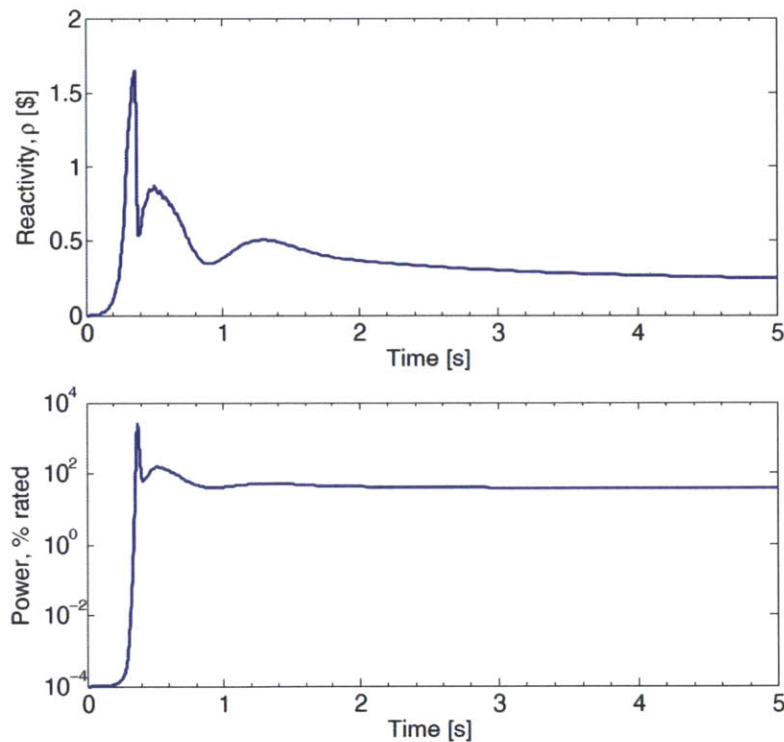
Figure 5.21, Reactivity and power variation

Hot rod search

The hot rod may be located by observing in Figure 5.22 the energy deposited in the fuel from the transient beginning $t = 0$ until the moment when critical condition is predicted by S3K. The highest LHGR occurs in pin (26,35). Similarly-high values of LHGR are recorded in the four pins located on row (26,35) on both sides of pin (26,35), and in pin (36,38).

From now on, we will refer to pin (26,35) as the hot rod.
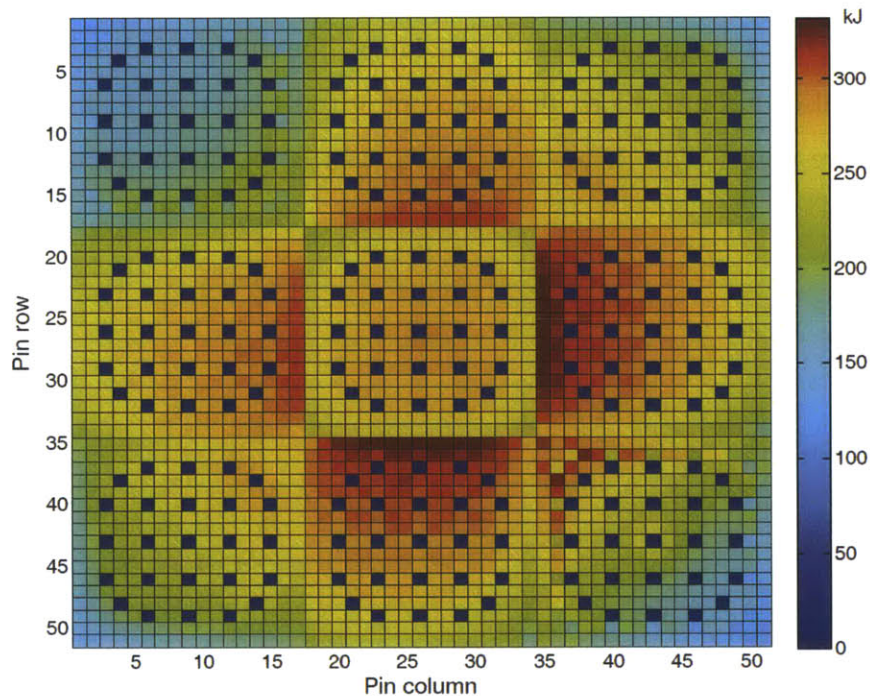
Figure 5.22, Pin energy deposited before the CHF point calculated by S3K

VIPRE recirculation mode

In this simulation, a converging solution could only be obtained by activating the recirculation mode of VIPRE, which is designed for problems with flow reversals. Such a mode is used for solving cases where fast velocity variations occur, and is expected to provide valid results for all simulations, even without fast velocity variations.

Hot rod analysis

The S3K power deposited in the hot rod is shown in Figure 5.23, and compared to the VIPRE power flowing through the cladding outside surface. Figure 5.24 shows the cladding outside temperature at the hot rod midplane.
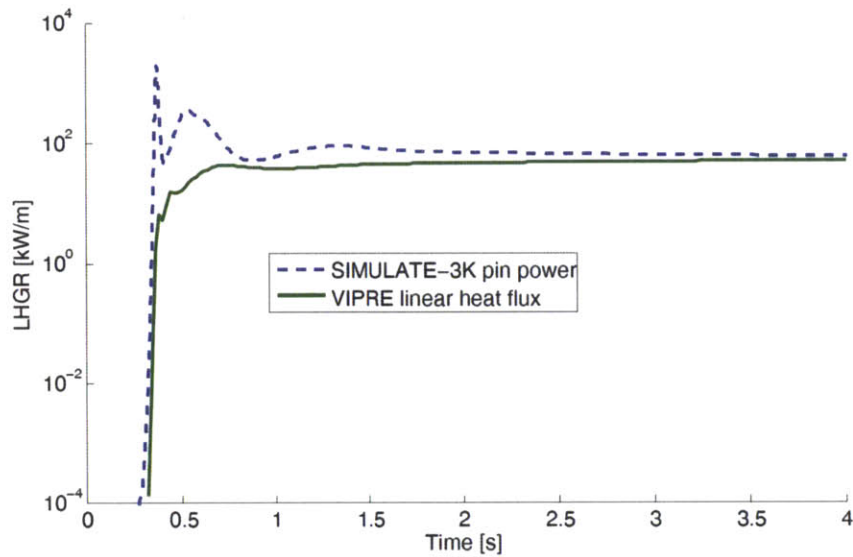
Figure 5.23, Hot rod axial midplane LHGR over time
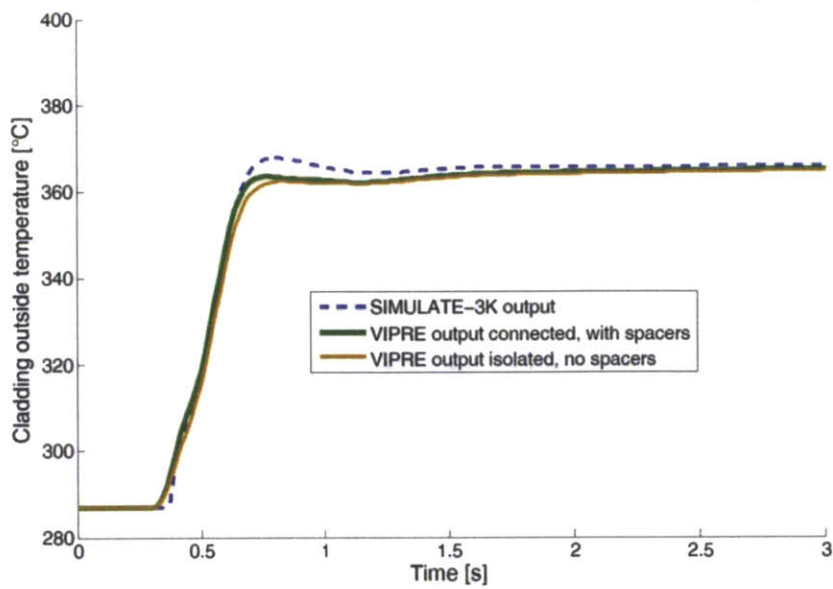
Figure 5.24, Outside cladding temperature at the hot rod axial midplane

A difference appears between the S3K and VIPRE temperatures plotted in Figure 5.24. Such an effect is probably due to the fact that the S3K model takes into account film boiling, which is enabled after DNB occurs around time $t = 0.6$ s. This deteriorates heat transfer and causes a cladding outside temperature increase. On the other hand, the VIPRE simulations have been done ignoring DNB and using a nucleate boiling heat transfer correlation even beyond the SS DNB point, as in Section 4.4.

In Figure 5.24 two VIPRE results have been plotted: an "isolated" one considering separated subchannels, and a "connected" one taking into account crossflow, spacer grids and turbulent mixing. The connected solution, just like in the standard benchmark case, presents a higher cladding outside temperature than the isolated one during the rapid temperature increase. Afterwards, the two temperatures become very similar.

Transient DNB explained test

The MDNBR, as shown in the top plot of Figure 5.25, has been obtained in two different ways, namely:

- Using the core minimum MDNBR determined by S3K

- Applying an external DNB routine to the VIPRE thermal-hydraulic results to calculate heat flux using the 2006 CHF look-up table of Groeneveld et al. (2007) in quasi-steady state. This has been done for both the connected and isolated VIPRE solution.

The three MDNBR trends shown in Figure 5.25 are all slightly different. This is probably due to the fact that the VIPRE solutions do not take into account film boiling after DNB, and to the fact that the VIPRE connected solution takes into account radial flow, turbulent mixing, and spacer grids, while the other two solutions compute the fluid parameters in isolated channels. Notice also that the DNBR value provided by S3K never gets lower than 1, while film boiling is enabled at DNBR=1.
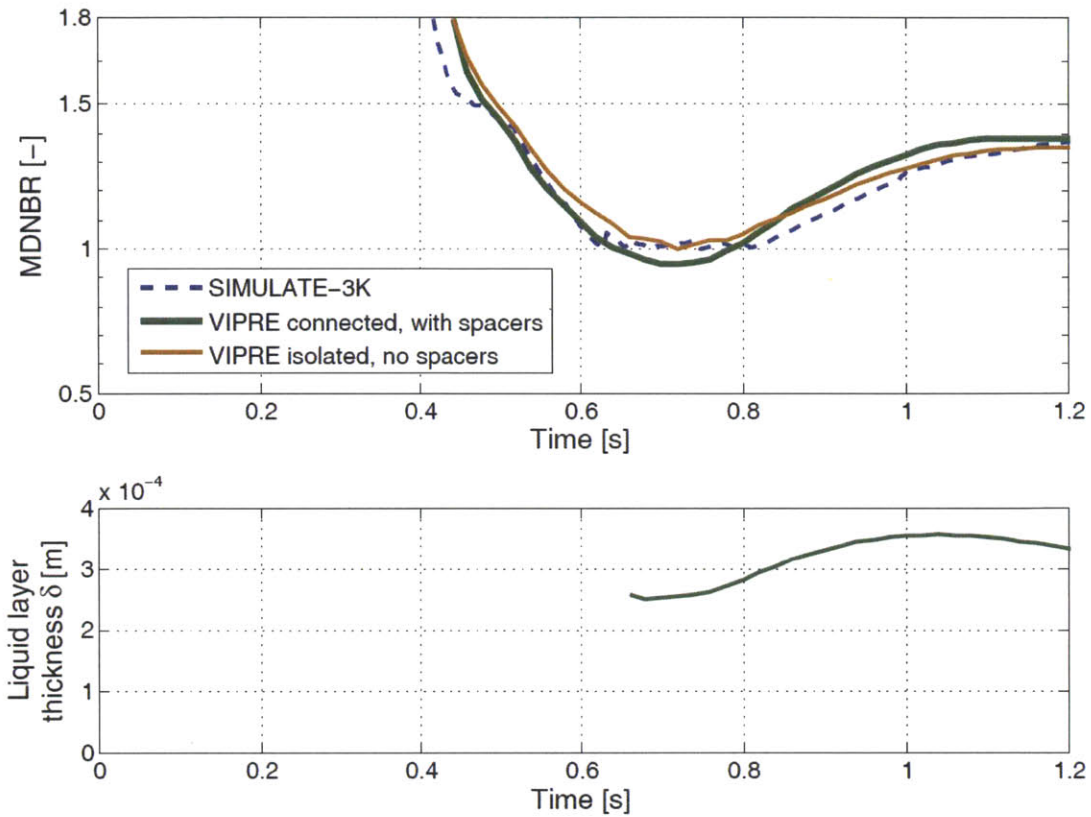
Figure 5.25, MDNBR and liquid layer thickness variation

A direct comparison can be made between the connected and the isolated DNBR results of Figure 5.25, since they use the same VIPRE structure and input data. The difference between the two MDNBR values is shown in Figure 5.26.

We can notice from Figure 5.26 that at the moment of DNB, which occurs at time $t = 0.65$ s, the isolated result predicts a MDNBR about 20% higher than the connected one, providing a more conservative estimate. Later on during the transient, around time $t = 0.9$s, the connected result becomes more conservative.

The transient DNB model has been tested on the connected results computed by VIPRE. Results are shown in the lower plot of Figure 5.25. After quasi-steady state DNB, the liquid layer thickness starts decreasing very slowly with time, but immediately after starts increasing again, without ever dropping to zero. This means that, while DNB

is predicted by quasi-steady state models to occur around time $t = 0.65$ s, the transient DNB formulation used does not predict any critical condition.
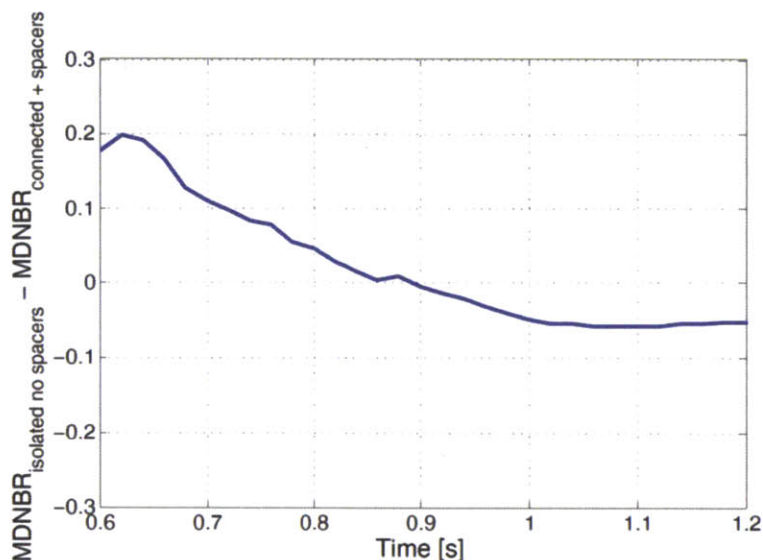
Figure 5.26, Comparison between the isolated and connected MDNBR results

5.5 Transient with 155.25% rod worth, ejection in 1 s

A case has been run setting the rod worth to 155.25% with respect to the benchmark specifications, and keeping the rod ejection time of 1 s, as in the previous case. Similar results as in the previous test were found regarding the hot rod location and cladding temperature variation with time.

MDNBR results are shown in the upper plot of Figure 5.27. We may notice that, similarly to what has been observed in the previous test, isolated results are more conservative than connected ones at the time of DNB. The two MDNBR curves cross over around time $t = 0.85$ s, when the connected result becomes more conservative.

84
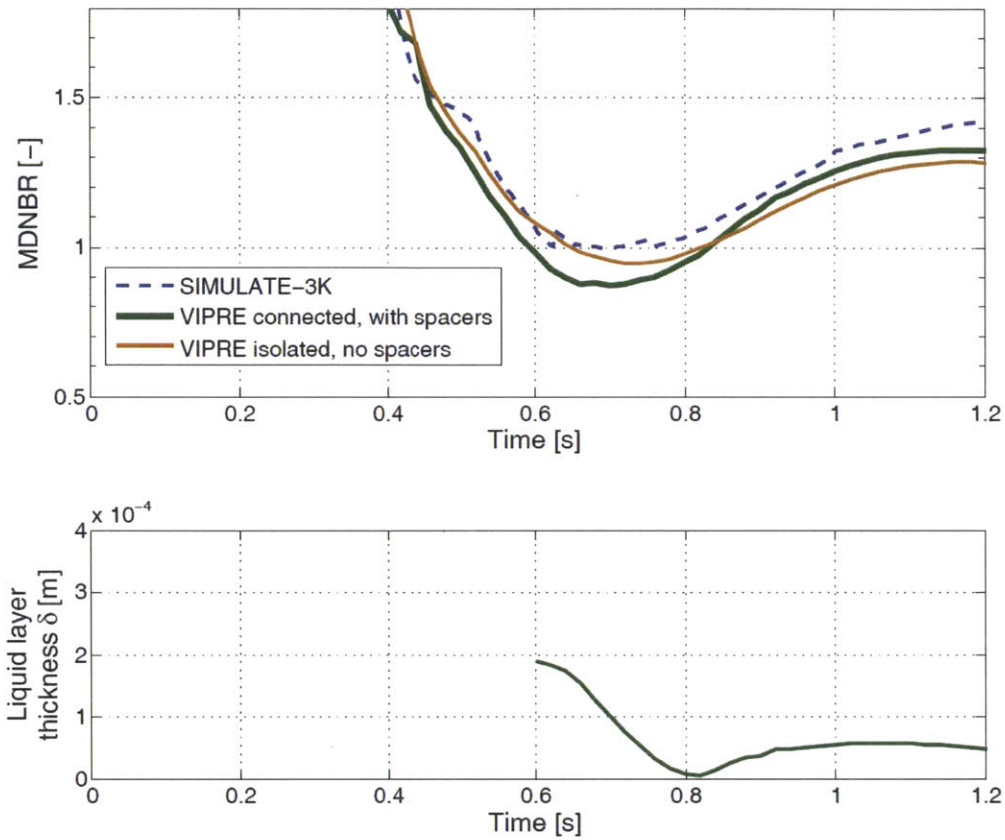
Figure 5.27, MDNBR and liquid layer thickness variation

In this test, MDNBR as calculated by the connected solution of VIPRE becomes smaller than 1, predicting quasi-steady state critical condition, at time $t = 0.6$ s. After this time, as shown in Figure 5.27, the liquid layer thickness decreases to almost zero in about 0.2 s, but then increases again. This is a case where transient DNB is not experienced, but a slightly higher rod power would lead to transient critical condition.

5.6 Transient with 155.30% rod worth, ejection in 1 s

Another case has been run with 1 s rod ejection time, and 155.30% rod worth with respect to the benchmark case. Since the rod worth is slightly higher than in the previous test, here we expect transient DNB to happen. Indeed, as shown in Figure 5.28, SS DNB

occurs at time $t = 0.6$ s, and the liquid layer thickness starts decreasing, initially driven by the HI model, and then by the thermal thinning one, until reaching zero at time $t = 0.78$ s. According to the model used, transient critical condition occurs 0.18 s after the DNB time predicted by the quasi steady-state model.
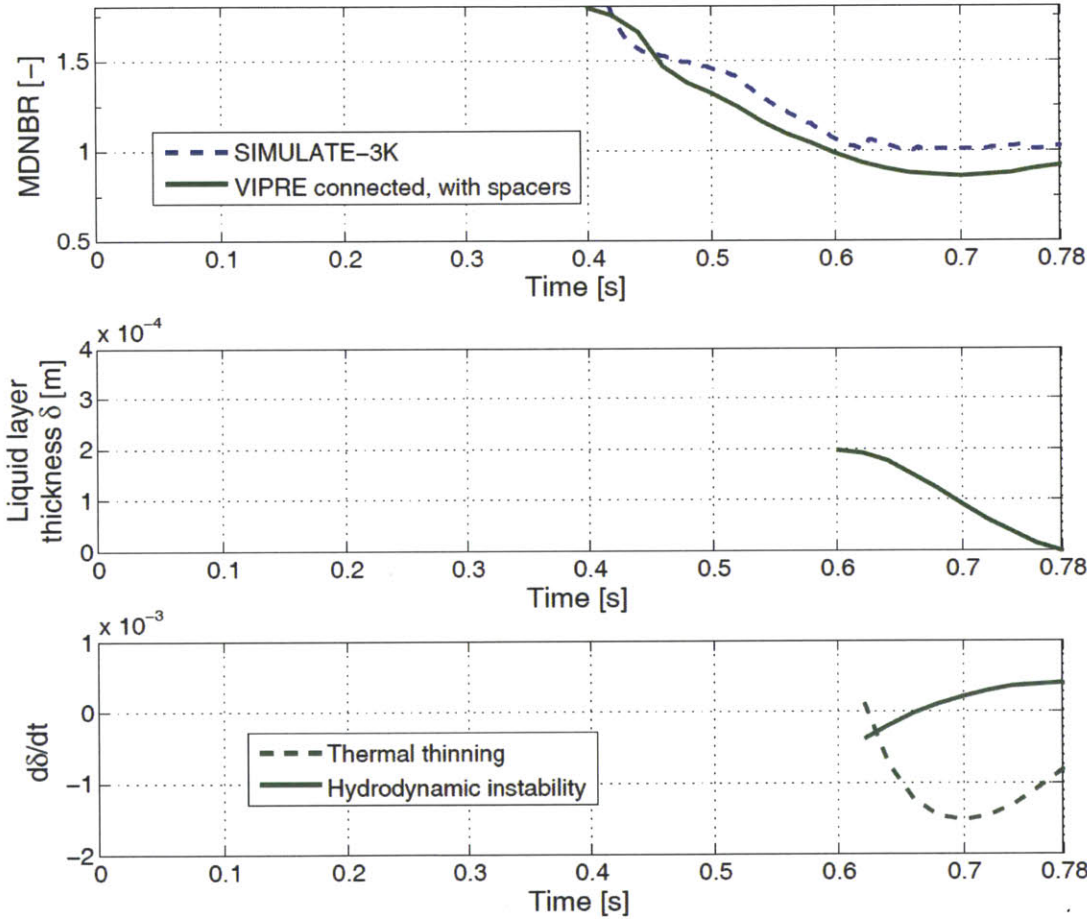
Figure 5.28, MDNBR, liquid layer thickness variation, and liquid layer thickness variation models

6 Conclusion

A theoretical approach for transient DNB has been adapted and generalized based on the model of Pasamehmetoglu et al. (1990b), to allow for application in reactor simulation codes. The resulting prediction approach has been validated against the low pressure experimental data of Kataoka et al. (1983). Then, the method has been applied to the simulation of PWR rod ejection accidents, assuming that validity still holds at higher pressure levels. The model has shown to be completely versatile and fully-applicable to PWR cases, providing realistic results.

The PWR rod ejection accident scenarios have been calculated using the reactor dynamics code SIMULATE-3K, together with its pin power reconstruction module. The pin power results from SIMULATE-3K have been used as an input to a thermal hydraulic simulation made with VIPRE, where thermal parameters have been evaluated with a subchannel radial resolution. The VIPRE model included crossflow between subchannels, turbulent mixing, and spacer grids, whose effect has been analyzed and compared for the rod ejection accident simulation. Lastly, the local thermal-hydraulic parameters calculated by VIPRE have been used in a routine to calculate DNB using both a quasi-steady state approach, and the transient DNB model.

The experimental and theoretical models on which this work is based show that very fast flow boiling power transients are conservatively but not accurately modeled by quasi steady-state DNB correlations. Some time is observed in experiments between the moment when DNB occurs as described by quasi steady-state approaches, and the effective critical condition. Such a time lag may be explained as the time required for the depletion of the liquid layer which exists between the heated wall and the bubbly layer.

The results deriving from the PWR rod ejection accident simulations show that a significant time difference exists between DNB as predicted by a quasi-steady state approach, and the critical condition predicted by the transient model. In some of the cases run in this work, DNB is only predicted by quasi-steady state approach, but does not occur when evaluated with the transient one.

6.1 Recommended future work

The following recommended tasks may lead to interesting results in future work:

- Experimental data may be collected at high pressure to allow for a full validation and calibration of transient DNB models at PWR operating pressure. It might be interesting to collect data not only for exponentially-increasing heat inputs as done by Kataoka et al. (1983), but also for different power variation shapes. For example, experiments done with a periodical power variation with different amplitudes would allow characterizing cases where transient DNB do not predict critical condition, but steady-state correlations do. Such a study may allow for the development of a robust model for transient DNB in PWR conditions.

- Transient models for evaluating the heat transfer coefficient both in single-phase forced convection and in nucleate boiling regime may be implemented, with the goal of refining DNB prediction capabilities.

- A model for HSN CHF at PWR pressure in forced convective heat transfer may be developed, using appropriate experimental data, to predict this kind of critical condition, which occurs at high subcooling.

- Tools for transient DNB prediction may be developed using CFD models.

- A more complete study may be done to evaluate the relative influence in subchannel analysis of grid spacers, turbulent interchange and crossflow, on the prediction of cladding outside temperature and DNBR.

7   References

CSAI, Vipre-01 Description, www.csai.com/vipre/vipre_whitepaper.pdf, accessed July 2012

Fukuda, K., Shiotsu, M., Sakurai, A. (2000) Effect of surface conditions on transient critical heat fluxes for a cylinder in a pool of water at pressures due to exponentially increasing heat inputs, *Nuclear Engineering and Design*, 200(1-2), 55-68

Grandi, G.M., Smith, K.S., Rhodes, J.D.III (2011) SIMULATE-3K Models and Methodology, SSP9813r7, Studsvik Scandpower (proprietary document), USA

Groeneveld, D.C., Shan, J.Q., Vasić, A.Z., Leung, L.K.H., Durmayaz, A., Yang, J., Cheng, S.C., Tanase, A. (2007) The 2006 CHF look-up table, *Nuclear Engineering and Design*, 237(15-17), 1909-1922

Haramura, Y., Katto, Y. (1983) A new hydrodynamic model of critical heat flux, applicable widely to both pool and forced convection boiling on submerged bodies in saturated liquids, *International Journal of Heat and Mass Transfer* 26(3), 389-399

Kataoka, I., Serizawa, A., Sakurai, A. (1983) Transient boiling heat transfer under forced convection, *International Journal of Heat and Mass Transfer* 26(4), 583-595

Kozlowski, T., Downar T.J. (2003) OECD/NEA and U.S. NRC PWR MOX/UO2 Core Transient Benchmark, Final Specifications Revision 2, OECD Energy Agency, USA

Kozlowski, T., Downar T.J. (2007) PWR MOX/UO2 Core Transient Benchmark, Final Report, OECD Energy Agency, USA

Pasamehmetoglu, K.O., Nelson, R.A., Gunnerson, F.S. (1990a) Critical Heat Flux Modeling in Pool Boiling for Steady-State and Power Transients, *Journal of Heat Transfer* 112(4), 1048-1057

Pasamehmetoglu, K.O., Nelson, R.A., Gunnerson, F.S. (1990b) Critical Heat Flux Modeling in Forced Convection Boiling for Steady-State and Power Transients, *Journal of Heat Transfer* 112(4), 1058-1062

Rempe, K.R., Smith, K.S., Henry, A.F. (1989) SIMULATE-3 pin power reconstruction: methodology and benchmarking, *Nuclear Science and Engineering* 103, 334-342

Sakurai A. (2000) Mechanisms of transitions to film boiling at CHFs in subcooled and pressurized liquids due to steady and increasing heat inputs, *Nuclear Engineering and Design*, 197(3), 301-356

Serizawa, A. (1983) Theoretical prediction of maximum heat flux in power transients, *International Journal of Heat and Mass Transfer*, 26(6), 921-932

Smith, K. (2012) Nuclear Reactor Physics class 22.211 lecture notes, MIT, Cambridge MA USA, Spring 2011

Stewart, C.W., Cuta, J.M., Montgomery, S.D., Kelly, J.M., Basehore, K.L., George, T.L., Rowe, D.S. (1989) VIPRE-01 A thermal-hydraulic code for reactor cores, Volume II: user's manual, EPRI-NP-2511-CCM-A, Revision 3, Electric Power Research Institute, USA

Sung, Y., Oelrich, R.L., Lee, C.C., Ruiz-Esquide, N., Gambetta, M., Mazufri, C.M. (2011) VIPRE-W Benchmark With PSBT Void and Temperature Test Data, Proceedings of NURETH-14, NURETH14-388, Toronto, Ontario, Canada, September 25-30, 2011

Todreas, N.E., Kazimi, M.S. (2011) Nuclear Systems, Volume 1, 2nd Edition, Taylor & Francis, Boca Raton, FL, USA

Tong, L. S., Weisman, J. (1996) Thermal analysis of pressurized water reactors , American Nuclear Society, La Grange Park, IL, USA

Zuber, N. (1959) Hydrodynamic aspects of boiling heat transfer, AECU-4439, United States Atomic Energy Commission, Los Angeles, CA, USA

8   Appendix A – CHF LUT correction factors

Table 8.1, Nuclear fuel bundle correction factors for the 2006 CHF Look-up table of Groeneveld et al. (2007). From Todreas and Kazimi (2011)

Factor	Form
K_1, Subchannel or Tube-Diameter Cross-Section Geometry Factor	For $3 < D_e < 25$ mm $\quad K_1 = (0.008 / D_e)^{1/2}$ For $D_e > 25$ mm: $\quad K_1 = 0.57$
K_2, Bundle-Geometry Factor	$$K_2 = \min\left[1, \left(\frac{1}{2} + \frac{2\delta}{D}\right)\exp\left(\frac{-(x_e)^{1/3}}{2}\right)\right]$$ where δ = minimum rod spacing[4] = $P - D$
K_3, Mid-Plane Spacer Factor for a 37-element Bundle (CANDU)	See [32]
K_4, Heated-Length Factor	For $L/D_e > 5$: $$K_4 = \exp\left[\left(\frac{D_e}{L}\right)\exp\left(2\alpha_{HEM}\right)\right]$$ $$\alpha_{HEM} = \frac{x_e\,\rho_f}{\left[x_e\,\rho_f + (1 - x_e)\,\rho_g\right]}$$
K_5, Axial Flux Distribution	For $x_e \leq 0$: $K_5 = 1.0$ For $x_e > 0$: $K_5 = q'' / q''_{BLA}$
K_6, Radial or Circumferential Flux Distribution Factor	For $x_e > 0$: $K_6 = q''(z)_{max} / q''(z)_{avg}$[4] For $x_e \leq 0$: $K_6 = 1.0$
K_7, Horizontal Flow-Orientation Factor	See [32]
K_8, Vertical Low-Flow Factor	$G < -400$ kg/m^2 s or $x << 0$: $\quad K_8 = 1$ $-400 < G < 0$ kg/m^2 s: $\quad$ See [32]

9 Appendix B – Benchmark pin geometry

All the information in this appendix is taken from the document containing the benchmark specifications (Kozlowski and Downar, 2003).

Table 9.1, Pin cell materials (Kozlowski and Downar, 2003)

\Cell Type Radius\	Fuel	IFBA	GT	CR	WABA
r0-r1	Fuel	Fuel	Water	Cr	Water
r1-r2	Gap	Ifba	Clad	Clad	Clad
r2-r3	Clad	Gap		Water	Waba
r3-r4		Clad		Clad	Clad
r4-r5					Water
r5-r6					Clad
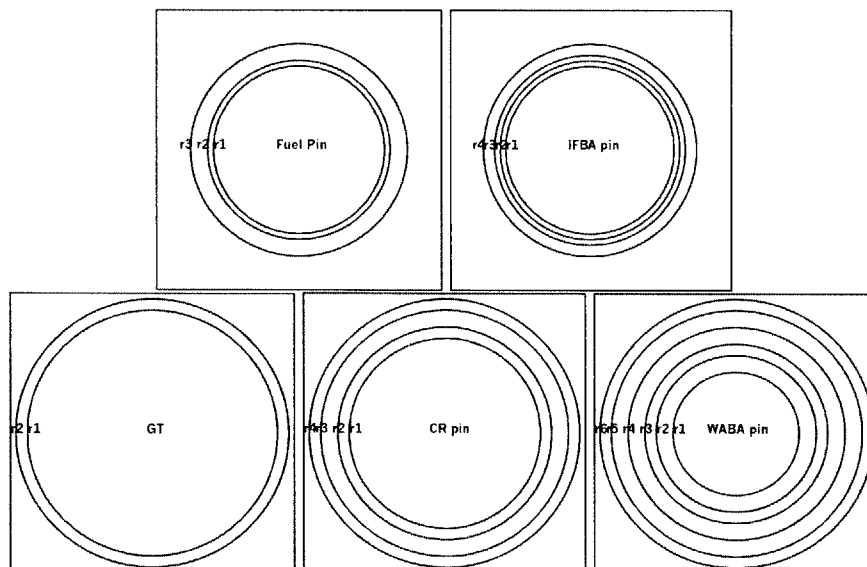
Figure 9.1, Pin cell geometry (Kozlowski and Downar, 2003)

Table 9.2, Pin cell dimensions [cm] (Kozlowski and Downar, 2003)

\Cell Type Radius\	Fuel	IFBA	GT	CR	WABA
r1	0.3951	0.3951	0.5624	0.4331	0.2858
r2	0.4010	0.3991	0.6032	0.4839	0.3531
r3	0.4583	0.4010		0.5624	0.4039
r4		0.4583		0.6032	0.4839
r5					0.5624
r6					0.6032

10 Appendix C – routines and input files

10.1 S3K input files

The reference S3K simulation used in this work is based on the OECD/NEA and NRC PWR MOX/UO$_2$ core transient benchmark (Kozlowski and Downar, 2003). The S3K input file for that benchmark has been generated by Studsvik Scandpower during summer 2005, and has been kindly provided by that company for this work.

The reference benchmark input file is not printed in this Appendix. However, the cards which have been modified from that input in this work are hereby shown.

Control rod ejection time

The card KIN.POS, shown in Listing 10.1, is used to modify the control rod ejection time. The benchmark specifications indicate a control rod ejection time of 0.1 s. That time has been increased in some of the tests in this work, to obtain a better stability of the VIPRE solution for cases with high reactivity insertion. For example, as underlined, the card in Listing 10.1 has an ejection time of 1.0 s.

Listing 10.1, Card to change the control rod ejection time

```
'KIN.POS'  9 3    0.0   0
                  1.0   225
                  100.0 225 /
```

Control rod worth multiplier

In some tests, the control rod worth has been modified. This is done through card KIN.MUL. In Listing 10.2, the control rod worth is set, as an example, to 1.55.

Listing 10.2, Card with the control rod worth multiplier

```
'KIN.MUL' 'RODOUT' 1.55 /
```

Core variable printing

The card KIN.PRI shown in Listing 10.3 is used to print the desired core parameters in the output file. The most important parameters in this work are:

ELAPT	Elapsed time [s]
APOW	Core power [MW]
CORPOW	Core power [% rated]
KEFF	K-effective
RHO$	Reactivity [$]
4PIN	Point-wise peaking factor
MDNBR	Minimum DNBR

Listing 10.3, KIN.PRI card for printing the desired core variables

```
'KIN.PRI' 1 ,, 'ELAPT' 'APOW' 'PEAK' 'CORPOW' 'KEFF' 'RHO' 'RHO$'
'2PIN' '1PIN' '4PIN' 'TFUAVE' 'TMOAVE' 'MDNBR' 'MDNBHF' 'DNBASS'
'TSRMX' 'TCLMX' 'IBOIL'/
```

Cards for pin power reconstruction

The cards EFP.OPT and EFP.FIL shown in Listing 10.4 are used respectively to perform pin power reconstruction over a specific set of 9 selected assemblies, and to print the results into a file. The option PPIN is selected in order to print tables of the relative pin power with respect to the core average. That option may be replaced with either PCPG or PTSR to provide the fuel enthalpy or the cladding outside temperature.

Listing 10.4, EFP cards for pin power reconstruction

```
'EFP.OPT' 'LOCAL' '2M001' '0U222' '1U502' '0U221' '2U213' '0U518'
'1U501' '0U517' '0M302' /
'EFP.FIL' 'ON' 'efpfile.dat' 'PPIN'/
```

10.2 Script to gather data from S3K EFP file

The pin power reconstruction data generated by S3K are printed in a proprietary format, which is processed by a routine provided by the code developer. Such a routine generates a text file with the desired data. The variables are read from the text file using a simple MATLAB routine shown in Listing 10.5. Such a routine can be used regardless if the output file contains data on relative pin power, cladding outside temperature, or fuel enthalpy.

Listing 10.5, Script to gather data from the pin power reconstruction output file

```
% variable | meaning
% ****************************
% np           pins
% nz,iz        vertical meshes
% nt,it        time steps
% na,ia        assemblies
% dum          dummy variable
% assynames    names of assemblies
% master       cell array containing data for each separate assembly
% master3      cell array containing data for 51x51 pin matrix
% times        vector with time steps [s]
% rowsmall     row on 17x17 matrix
```

```matlab
% colsmall      column on 17x17 matrix
% rowbig        row on 51x51 matrix
% colbig        column on 51x51 matrix

clear all

assynames = {'2M001' '0U222' '1U502',...
             '0U221' '2U213' '0U518',...
             '1U501' '0U517' '0M302'};


na=9;
np=17;
nz=24;


readfile = fopen('efpfile.out','r');

%CHECK FOR TAG 'COUNT'
dum = fscanf(readfile,'%s',1);
if ~strcmp('COUNT', dum)
    error('ERROR IN READING COUNT');
end

nt = fscanf(readfile,'%d',1);

%MAIN MASTER CELL AND VECTOR WITH TIME
master = cell(nz,nt,na);
times = zeros(nt,1);

%TIME STEPS
LOOP************************************************************
for it=1:nt

    %CHECK FOR TAG 'ELAPT'
    dum = fscanf(readfile,'%s',1);
    if ~strcmp('ELAPT', dum)
        error('ERROR IN READING ELAPT');
    end
    %READ TIME
    times(it) = fscanf(readfile,'%f',1);

%ASSEMBLY
LOOP************************************************************
for ia=1:na

%Z POSITIONS
LOOP************************************************************
for iz=1:nz

    dum = fscanf(readfile,'%s',1);
    if ~strcmp('LABEL', dum)
        error('ERROR IN READING LABEL');
    end
```

```matlab
    %READ ASSY and AXIAL POS
    dum = fscanf(readfile,'%s',1);
    iztest = fscanf(readfile,'%d',1);

        %test the name of assembly
        iatest=0;
        for i=1:na
        if strcmp(assynames{i}, dum)
            iatest=i;
        end
        end
        if iatest==0
            error('ERROR IN READING ASSY NAME');
        end
        if ia~=iatest
            error('ERROR IN ASSY NAME TEST');
        end
        %test the z position
        if iz~=iztest
            error('ERROR IN Z POSITION TEST');
        end

    %SCAN THE MATRIX
    master{iz,it,ia}=transpose(fscanf(readfile,'%f',[np,np]));

end
end
end


%**********************************************************************
***
% Part 2 - create only one array, 51x51

master3 = cell(nz,nt);   %array to be created
for it=1:nt
for iz=1:nz

master3{iz,it} = zeros(51); % preallocate the 23x23 matrix


for ia=1:na

    assycol=mod(ia-1,3)+1;
    assyrow=(ia-assycol)/3+1;

    rowsmall = 1:17 %Rows and columns in the 17x17 matrix
    colsmall = 1:17

    rowbig=rowsmall+17*(assyrow-1); %Rows and columns in the 51x51
matrix
    colbig=colsmall+17*(assycol-1);
```

```
    master3{iz,it}(rowbig,colbig) =
master{iz,it,ia}(rowsmall,colsmall);

    end
    end

if mod(it,10)==0
fprintf('timestep %d out of %d done\n', it,nt); %Print status
end

end

save('times.mat'); %Save the scanned variables in a file

fclose(readfile);
```

10.3 Script to elaborate data for VIPRE input file

The script shown in Listing 10.6 reads the pin power variables and saves them in a text file in the format required by the VIPRE input. Two files are written:

- A file containing the global average LHGR as a function of time. Since the VIPRE analysis is only done in 9 assemblies of interest and not in the whole core, the global average LHGR here is the average in the assemblies of interest.

- A file containing the local power profiles at every time step, pin, and axial location. Local power profiles are all expressed as a fraction of the average LHGR provided in the previous file.

Listing 10.6, Script to write the pin power data in the VIPRE input format

```
% Variables not already listed in the previous section.
%
% variable | meaning
% ***************************
% timesteps    number of time steps in the S3K output
% times        vector with the time steps
% pinpower     pin power map
% tempvect     temporary storage vector
% matrix3davgpinpower
% dum          dummy variable
```

```
% profile      local power factors
%
% Subscript 0 refers to the S3K time steps, while subscript 1 refers to
% a vector with a reduced number of time steps
%
% The file avgpower.mat has been saved containing the average core LHGR
% in kW/ft/rod at every time step, and the time step vector,
% respectively in the two variables avgassypower and avgassytime.
% Those vectors are elaborated from the S3K output.

clear all

load('avgpower.mat');
load('times.mat');

%###############################################################
%FIND NUMBER OF TIME STEPS
datanum=size(master3); %find number of time steps in data file

timesteps_0=datanum(2);    %time steps in data file
timesteps_1=100;           %desired number of time steps
times(timesteps_0-1)=5;    %correct %INSERTFINALTIMEHERE

    if mod(timesteps_1,4)~=0
        error('ERROR,: TIMESTEPS_1 SHOULD BE A MULTIPLE OF 4')
    end

%###############################################################
%CREATE THE TIME VECTOR WITH FEWER TIME STEPS
times_1_interpoints=1+(timesteps_0-1)*((1:timesteps_1)-1)/(timesteps_1-
1);
times_1=interp1(1:timesteps_0,times,times_1_interpoints);

% Fix last time step
avgassypower(timesteps_0)=avgassypower(timesteps_0-1);
avgassytime(timesteps_0)=avgassytime(timesteps_0-1);

% Create 51x51 pin matrices
pinpower_0 = zeros ( 51, 51 , nz , timesteps_0 );
pinpower_1 = zeros ( 51, 51 , nz , timesteps_1 );

%###############################################################
%CREATE A 4D MATRIX WITH ALL DATA

for it=1:timesteps_0
for iz=1:nz
for row = 1:51
for col = 1:51
 pinpower_0(row,col,iz,it)=avgassypower(it)*master3{iz,it}(row,col);
end
end
end
end
```

```
%#################################################################
%INTERPOLATE THE VALUES ON FEWER TIME STEPS

for iz=1:nz
for row = 1:51
for col = 1:51

    tempvect_0 = squeeze(pinpower_0(row,col,iz,:));
    tempvect_1 = interp1(times,tempvect_0,times_1);

    for it = 1:timesteps_1
        pinpower_1(row,col,iz,it)=tempvect_1(it);
    end

end
end
end

%#################################################################
% CALCULATE NUMBER OF FUEL PINS AND POSITION OF NONFUEL RODS

npins = 0;
fuelrods = 0;
nonfuelrod = zeros (51^2,1);
for row = 1:51
for col = 1:51
    npins = npins + 1;
    if pinpower_1(row,col,1,1)~=0
        fuelrods = fuelrods+1;
    else
        nonfuelrod(npins) = 1;
    end
end
end

%#################################################################
%MATRIX WITH AVG POWER

matrix3davgpinpower_1 = zeros(timesteps_1,1);
for it=1:timesteps_1
    dum3 = zeros(nz,1);
    for iz=1:nz
    dum=pinpower_1(:,:,iz,it);
    dum2=sum(dum);
    dum3(iz)=sum(dum2);
    end
    matrix3davgpinpower_1(it)=sum(dum3)/(fuelrods*nz);
end

matrix3davgpinpower_0 = zeros(timesteps_0,1);
for it=1:timesteps_0
    dum3 = zeros(nz,1);
    for iz=1:nz
    dum=pinpower_0(:,:,iz,it);
```

```matlab
        dum2=sum(dum);
        dum3(iz)=sum(dum2);
        end
    matrix3davgpinpower_0(it)=sum(dum3)/(fuelrods*nz);
end
matrix3davgpinpower_0_metric = matrix3davgpinpower_0*3.28084;

%############################################################
%WRITE TEXT FILE WITH AVERAGE POWER

decks=floor(timesteps_1/4)+1;
dum=1;

txt = fopen('assypower.txt','wt');
fprintf(txt,'\nThe file contains %d data points\n\n\n\n',timesteps_1);


for i=1:decks
for j=1:4

    if dum<=timesteps_1
        fprintf(txt,'%f,%f,',times_1(dum),matrix3davgpinpower_1(dum));
    end
    dum=dum+1;
end
    fprintf(txt,'\n');
end

fclose(txt);

%############################################################
%WRITE TEXT FILE WITH PIN POWER PROFILES

profile=zeros(51^2,nz,timesteps_1); %3D PEAKING FACTORS ARRAY
dum3=zeros(timesteps_1,1);              %RELATIVE TO AVG

    for iz=1:24
        for row=1:51
            for col=1:51
                rod=(row-1)*51+col;
                for it=1:timesteps_1

                    profile(rod,iz,it)=pinpower_1(row,col,iz,it)...
                        /matrix3davgpinpower_1(it);
                end
            end
        end
    end

% This part prints the power profile tables

txtfile = fopen('viprepowertables.txt','wt');
```

```matlab
for ip=1:51^2

    if profile(ip,12,timesteps_1/2)~=0

            for it=1:timesteps_1

                fprintf(txtfile,'24  *rods3+rods4\n');

                for i1z=1:6
                    for i2z=1:4

                        fprintf(txtfile,'%f,',6*(4*(i1z-1)+i2z)-3);
                        fprintf(txtfile,'%f,',profile...
                            (ip,(4*(i1z-1)+i2z),it));
                    end
                    fprintf(txtfile,'\n');
                end

            end
    end
end


        iii=1;

for ip=1:51^2

    if profile(ip,12,timesteps_1/2)~=0

        fprintf(txtfile,'%d  *rods7+rods8\n', timesteps_1);


        if mod(timesteps_1,4)~=0
            error('ERROR, TIMESTEPS NOT MULTIPLE OF 4 CHANGE CODE')
        end

        ttt=1;

        for i1t=1:timesteps_1/4
        for i2t=1:4
            fprintf(txtfile,'%f,',times_1(ttt));
            fprintf(txtfile,'%d,',iii);
            iii=iii+1;
            ttt=ttt+1;
        end
        fprintf(txtfile,'\n');
        end
    end
end

fclose(txtfile);
```

10.4 VIPRE input file

The VIPRE input file contains information needed for the subchannel calculation, and is hereby illustrated. The main input parameters are listed in a bulleted list at the beginning of each section.

Initial and Geometry cards

- 2704 subchannels

- 24 axial levels

- 144 in. heated length

Listing 10.7, Initial and Geometry VIPRE cards

```
*  (page 2-5)
1,0,0                                                              *vipre.1
3x3 assembly pin-by-pin PWR RIA simulation
*vipre.2
*  (page 2-11)
geom,2704,2704,24,0                                                *geom.1
144.,0.,0.3746                                                     *geom.2
*
*
*Schl   A          Pw          Ph  gaps (g# centroid dist, P)x gaps      *geom.4
1,0.035950,0.283423,0.283423,2,2,0.067598,0.496062,53,0.067598,0.496062
2,0.071900,0.566846,0.566846,2,3,0.067598,0.496062,54,0.135197,0.496062
3,0.071900,0.566846,0.566846,2,4,0.067598,0.496062,55,0.135197,0.496062
4,0.071900,0.566846,0.566846,2,5,0.067598,0.496062,56,0.135197,0.496062
*(similar entry for each of 2704 subchannels)
2701,0.071900,0.566846,0.566846,1,2702,0.067598,0.496062
2702,0.071900,0.566846,0.566846,1,2703,0.067598,0.496062
2703,0.071900,0.566846,0.566846,1,2704,0.067598,0.496062
2704,0.035950,0.283423,0.283423,0
*
```

Operating conditions cards

- 548.33 °F uniform inlet temperature (equivalent to 560 K)

- 2248.1 psi operating system pressure (equivalent to 15.5 MPa)

- 2.5 % of heat is generated in the coolant (typical value)

- 2.3636 $lb_m/hr\text{-}ft^2$ uniform inlet mass flux (equivalent to 801.34 kg/m^2s)

- 0.000008 initial average LHGR in the assemblies of interest, in the VIPRE units of kW/ft, as derived from S3K

- 100 time steps for time-dependent average LHGR distribution

Listing 10.8, Operating conditions VIPRE cards

```
* (page 2-125)
oper,1,2,0,0,0,1,0,                                            *oper.1
0., 0., 2.5, 0.0005                                           *oper.2
*p_oper,T_in,G_in,q'core-ave(kW/ft)
2248.1,548.33,2.3636,0.000008,                               *oper.5
0,0,0,-100,0,0,                                               *oper.12
*
*ASSY POWER
*(insert here tables of average power)                        *oper.20
*
```

Computational control VIPRE cards

- 3.0 s total transient time

- 1000 minimum number of time steps

- Adjust time step size automatically based on rate of change of forcing functions

- 20 maximum external iterations

- 50 maximum internal iterations for energy equation and pressure solution

- 2 minimum internal iterations

- Recirculation module activated

- 0.25 crossflow convergence limit

- 0.0001 pressure convergence limit (suggested by user manual)

- 0.01 axial flow convergence limit (suggested by user manual)

- 0.05 °F rod temperature convergence limit (suggested by user manual)

- 0.01 heat transfer coefficient convergence limit (suggested by user manual)

- 0.9 damping factor for crossflow solution (suggested by user manual)

- 1.0 damping factor for axial flow

Listing 10.9, Computational control VIPRE cards

```
*
cont                                                          *cont.1
*transient time, min # of time steps, max external iterations
3.0,1000,20,50,2,2,0,0                                       *cont.2
*0.25,0.0001,0.01,0.05,0.01,0.9,1.5,1.0                      *cont.3
0.1,0.0001,0.01,0.05,0.01,0.9,1.0,1.0                        *cont.4
0,9,2,10,4,0,1,1,0,0,0,1                                     *cont.6
15000.0,0.05,5.0,0.5,5.0,5.0,                               *cont.7
1843,1844,1845,1846,1847,1848,1849,1850,1859 *channels printed *cont.8
1759,1846 *gaps printed                                     *cont.9
1756,1757,1758,1759,1760,1761,1762,1763,1764,1923 *rods printed*cont.10
1845,1848,2013,2012  *dnb results printed                   *cont.11
*
```

Fluid properties

Fluid properties are calculated by direct solution of EPRI curve-fit functions for water properties. In PWR applications pressure drops are negligible compared to the system pressure. Therefore, all fluid properties are calculated at reference pressure.

Listing 10.10, Fluid properties VIPRE card

```
* (page 2-54)
prop,0,0,2,0      * internal EPRI functions                  *prop.1
*
```

Correlation selection

- Levy model for subcooled void

- Homogeneous model for bulk void/quality

- Homogeneous model for two-phase friction multiplier

- Dittus-Boelter correlation, modified for turbulent flow, for single-phase forced convection heat transfer, using coefficient 0.03126 for the Reynolds number.

- Chen correlation for subcooled nucleate boiling heat transfer

- Chen correlation for saturated nucleate boiling heat transfer

Listing 10.11, Rods and End of input VIPRE cards

```
*
*corr,0,1     *# of CHF corrs, 1-only to boiling point , page2-154
*corr.1
levy,homo,homo,none,    *subcool, bulk, 2-ph mult, hot wall      *corr.2
epri,chen,chen,epri,                                             *corr.6
0.03216,                                                         *corr.7
0,0,0.0                                                          *corr.16
*
```

Turbulent mixing correlations

Some cards in VIPRE allow defining the exchange of energy and momentum between adjacent channels due to turbulent mixing. This calculation is not done through a complete turbulence model, but through empirical correlations. A turbulent momentum factor, FTM, is used to quantify to which extent turbulent crossflow mixes momentum as well as enthalpy. If FTM equals zero, only enthalpy is mixed by the crossflow, while if FTM equals one, momentum is mixed with the same strength as enthalpy.

The turbulent crossflow w' is calculated using the correlation in Eq. (10.1), where S is the width of the gap between neighboring subchannels, in length units, and $\bar{G}$ is the

average mass flux between the two neighboring subchannels. A mixing coefficient A_β is taken as equal to 0.07, as suggested by a Benchmark of VIPRE made using PWR bundle measurements (Sung et al., 2011).

$$w' = A_\beta \cdot S \cdot \bar{G}$$ (10.1)

Listing 10.12, Turbulent mixing VIPRE cards

```
* (page 2-174)
mixx,0,0,0                                              *mixx.1
0.8,0.07                                                *mixx.2
*
```

Friction input

The Blasius smooth tube correlation, which is the VIPRE default friction correlation, is used. Lateral resistance to crossflow is calculated applying a constant loss coefficient to all subchannel connections, which is set equal to 0.5, as recommended by the VIPRE user manual (Stewart et al., 1989) for subchannel analysis.

The lateral loss coefficient K determines the crossflow resistance as in Eq. (10.2), from Stewart et al., (1989).

$$\frac{dp}{dy} = \frac{K|w_j|w_j}{2S}$$ (10.2)

In Eq. (10.2), w_j is the crossflow through a gap, and S is the gap width.

Listing 10.13, Friction VIPRE cards

```
* (page 2-179)
drag,0,0,0                                              *drag.1
0.5,                                                    *drag.5
*
```

Spacer grids

- 0.8 constant local loss coefficient

- 7 axial locations

- Axial locations, in inches: 12,32,52,772,92,112,132

Listing 10.14, Spacer grid VIPRE cards

```
*
grid,0,1        * 0-local, # of correlations, page2-192              *grid.1
.80                                                                  *grid.2
-1,7            * all channels have same cd = .80                    *grid.4
12.0,1,32.0,1,52.0,1,72.0,1,92.0,1,112.0,1,? * grid loc.            *grid.6
132.0,1,                                                             *grid.6
0,                                                                   *grid.4
*
```

Rods cards and End of input

This section contains input information about the fuel rods, their power generation profiles, and their properties. The assemblies of interest contain 2,376 fuel rods out of 2,601 total rods. A number of time-varying axial power shapes equal to the number of fuel rods is provided as an input. Multiplying this by 100 time steps leads the number of axial power profile tables needed to describe the transient, which is 236,700.

- 2,601 total number of rods

- 2,376 time-varying axial power shapes

- 236,700 axial power profile tables

- 0.4750 in. outer diameter of nonfuel pins

- 0.3609 in. outer diameter of fuel pins

- 0.3111 in. fuel pellet outer radius

- 6 radial nodes in the fuel pellet

- 0.02256 in. cladding thickness

- Assume uniform radial power profile in the fuel pellet

- Properties for UO2 fuel, MOX fuel and cladding provided in a table derived from the property relations given in the Benchmark specifications

- 1761.1 Btu/hr-ft^2-°F Constant gap conductance (equivalent to 1.000 W/cm^{2}K)

Listing 10.15, Rods and End of input VIPRE cards

```
* (page 2-62)
rods,237600,2601,1,3,3,0,0,0,2376                                    *rods.1
*
0.0,0.0,0,1    *zheat=zbundle,zstart power prof., page2-67          *rods.2
*
*axial power profile tables
24
*rods.3+rods.4
6.0000,0.180619,12.0000,0.322857,18.0000,0.468105,24.0000,0.606579,
30.0000,0.735271,36.0000,0.852673,42.0000,0.956529,48.0000,1.046086,
54.0000,1.119086,60.0000,1.175530,66.0000,1.213159,72.0000,1.231973,
78.0000,1.231973,84.0000,1.213159,90.0000,1.175530,96.0000,1.119086,
102.0000,1.046086,108.0000,0.956529,114.0000,0.852673,120.0000,0.735271
,
126.0000,0.606579,132.0000,0.468105,138.0000,0.322857,144.0000,0.180619
,
*(entry rods3+rods4 is repeated for each of 285120 power profile
tables)
*
*time-varying axial power shapes
120
*rods.7+rods.8
0.000000,1,0.008584,2,0.013897,3,0.018422,4,
0.022591,5,0.026516,6,0.030298,7,0.033969,8,
0.037571,9,0.041127,10,0.044705,11,0.048325,12,
0.051993,13,0.055742,14,0.059626,15,0.063629,16,
*(entry rods7+rods8 is repeated for each of 2376 time-varying shapes)
*
*rod id, associated axial power table, and fraction of power to channel
1,2,1,1,1,0.25,2,0.25,53,0.25,54,0.25                              *rods.9
2,2,1,2,2,0.25,3,0.25,54,0.25,55,0.25
3,2,1,3,3,0.25,4,0.25,55,0.25,56,0.25
4,2,1,4,4,0.25,5,0.25,56,0.25,57,0.25
*(similar entry for each of 2601 rods)
2598,2,1,2373,2648,0.25,2649,0.25,2700,0.25,2701,0.25
```

```
2599,2,1,2374,2649,0.25,2650,0.25,2701,0.25,2702,0.25
2600,2,1,2375,2650,0.25,2651,0.25,2702,0.25,2703,0.25
2601,2,1,2376,2651,0.25,2652,0.25,2703,0.25,2704,0.25
0
*         Dco   Dfo #nodes_r Dfi t_clad
* DUMMY
1,dumy,0.4750                                              *rods.68
* UO2 FUEL
2,nucl,0.3609,0.3111,6,0.,0.02256                          *rods.62
0,2,1,0,0,1761.1,1,0.0                                     *rods.63
* MOX FUEL
3,nucl,0.3609,0.3111,6,0.,0.02256                          *rods.62
0,3,1,0,0,1761.1,1,0.0                                     *rods.63
*
*
*MATERIAL PROPERTIES rods.70 and rods.71
1,30,406.031,clad
536,0.07548,9.20555,626,0.07685,9.54730,
716,0.07822,9.88726,806,0.07959,10.22875,
896,0.08096,10.57509,986,0.08233,10.92960,
1076,0.08370,11.29562,1166,0.08507,11.67646,
1256,0.08644,12.07544,1346,0.08781,12.49589,
1436,0.08918,12.94114,1526,0.09055,13.41451,
1616,0.09192,13.91932,1706,0.09329,14.45889,
1796,0.09466,15.03656,1886,0.09603,15.65563,
1976,0.09740,16.31945,2066,0.09877,17.03132,
2156,0.10014,17.79458,2246,0.10151,18.61255,
2336,0.10288,19.48855,2426,0.10425,20.42590,
2516,0.10562,21.42793,2606,0.10699,22.49797,
2696,0.10836,23.63933,2786,0.10973,24.85534,
2876,0.11110,26.14933,2966,0.11247,27.52461,
3056,0.11384,28.98452,1000000,0.11522,30.53237,
*
2,50,639.262,uo2f
536,0.06402,3.19470,626,0.06511,2.95054,
716,0.06606,2.74849,806,0.06687,2.57850,
896,0.06756,2.43352,986,0.06813,2.30839,
1076,0.06860,2.19931,1166,0.06898,2.10336,
1256,0.06929,2.01833,1346,0.06953,1.94243,
1436,0.06971,1.87428,1526,0.06985,1.81275,
1616,0.06995,1.75691,1706,0.07004,1.70601,
1796,0.07011,1.65943,1886,0.07019,1.61664,
1976,0.07028,1.57719,2066,0.07040,1.54070,
2156,0.07055,1.50686,2246,0.07075,1.47538,
2336,0.07101,1.44604,2426,0.07134,1.41861,
2516,0.07175,1.39291,2606,0.07226,1.36880,
2696,0.07287,1.34611,2786,0.07360,1.32474,
2876,0.07446,1.30457,2966,0.07545,1.28550,
3056,0.07660,1.26745,3146,0.07791,1.25033,
3236,0.07939,1.23408,3326,0.08106,1.21862,
3416,0.08293,1.20391,3506,0.08500,1.18989,
3596,0.08730,1.17652,3686,0.08982,1.16374,
3776,0.09259,1.15153,3866,0.09562,1.13983,
3956,0.09890,1.12863,4046,0.10247,1.11789,
```

```
4136,0.10633,1.10759,4226,0.11048,1.09769,
4316,0.11495,1.08817,4406,0.11974,1.07902,
4496,0.12486,1.07021,4586,0.13034,1.06172,
4676,0.13616,1.05353,4766,0.14236,1.04564,
4856,0.14894,1.03802,1000000,0.15591,1.03066,
*
3,50,649.875,moxf
536,0.06402,2.87523,626,0.06511,2.65549,
716,0.06606,2.47364,806,0.06687,2.32065,
896,0.06756,2.19016,986,0.06813,2.07755,
1076,0.06860,1.97938,1166,0.06898,1.89303,
1256,0.06929,1.81649,1346,0.06953,1.74819,
1436,0.06971,1.68685,1526,0.06985,1.63147,
1616,0.06995,1.58122,1706,0.07004,1.53541,
1796,0.07011,1.49349,1886,0.07019,1.45497,
1976,0.07028,1.41947,2066,0.07040,1.38663,
2156,0.07055,1.35617,2246,0.07075,1.32785,
2336,0.07101,1.30143,2426,0.07134,1.27675,
2516,0.07175,1.25362,2606,0.07226,1.23192,
2696,0.07287,1.21150,2786,0.07360,1.19227,
2876,0.07446,1.17411,2966,0.07545,1.15695,
3056,0.07660,1.14070,3146,0.07791,1.12530,
3236,0.07939,1.11067,3326,0.08106,1.09676,
3416,0.08293,1.08352,3506,0.08500,1.07091,
3596,0.08730,1.05887,3686,0.08982,1.04737,
3776,0.09259,1.03637,3866,0.09562,1.02585,
3956,0.09890,1.01577,4046,0.10247,1.00610,
4136,0.10633,0.99683,4226,0.11048,0.98792,
4316,0.11495,0.97935,4406,0.11974,0.97112,
4496,0.12486,0.96318,4586,0.13034,0.95554,
4676,0.13616,0.94818,4766,0.14236,0.94107,
4856,0.14894,0.93421,4946,0.15591,0.92759,
*
endd
0
```

All the cards above have been included in a single input file and run using the VIPRE license of MIT.

10.5 Script to gather data from VIPRE output file

The following simple MATLAB script reads the data in the VIPRE output file and stores them in variables which are used by the transient DNB routine.

Listing 10.16, MATLAB script to gather data from the VIPRE output file

```
% variable | meaning
% ***************************
% chofint      channels of interest
% rod of int  rods of interest
% hf           heat flux
% cot          cladding outside temperature
% fenth        fuel enthalpy
% m            mass flux
% h            heat transfer coefficient
% tempvect     temporary storage vector
% matrix3davgpinpower
% dum          dummy variable
% profile      local power factors


clear all


chofint = [1843,1844,1845,1846,1847,1848,1849,1850,1859];
rodofint = [1756,1757,1758,1759,1760,1761,1762,1763,1764,1923];


[dum,nchi]=size(chofint);
[dum,nrodi]=size(rodofint);


for irodi=1:nrodi
irodi
ofile = fopen('outptt','r');
it=0;

%++++++++++++++++++++++++++++++++++++++++++++++++++++++++++++
while ~feof(ofile)

% search for Beginning of data
dum = fscanf(ofile,'%s',1);
if
(strcmp(dum,'iterative')||strcmp(dum,'direct')||strcmp(dum,'recirc'))
dum = fscanf(ofile,'%s',1);
if strcmp(dum,'solution')
dum = fscanf(ofile,'%s',1);
if strcmp(dum,'(idrect')
```

```
dum = fscanf(ofile,'%s',1);
if strcmp(dum,'=')
dum = fscanf(ofile,'%s',1);
if strcmp(dum,'2)')
dum = fscanf(ofile,'%s',1);
if strcmp(dum,'-')
dum = fscanf(ofile,'%s',1);
if strcmp(dum,'time')
dum = fscanf(ofile,'%s',1);
if strcmp(dum,'=')

it=it+1;
time(it) = fscanf(ofile,'%f',1);


%========================================================
% Search for the rod of interest
stop=0;
while stop==0
    dum = fscanf(ofile,'%s',1);
    if strcmp(dum,'rod')
    dum = fscanf(ofile,'%s',1);
    if strcmp(dum,'no.')
    rod = fscanf(ofile,'%d',1);
    if rod==rodofint(irodi)
        stop=1;

%     within the rod of interest, read the data
stop2=0;


%$$$$$$$$$$$$$$$$$$$$$$$$$$$$$Search for beginning of matrix
while stop2==0
    dum = fscanf(ofile,'%s',1);
    if strcmp(dum,'line')
    dum = fscanf(ofile,'%s',1);
    dum = fscanf(ofile,'%s',1);
    dum = fscanf(ofile,'%s',1);
    dum = fscanf(ofile,'%s',1);
    dum = fscanf(ofile,'%s',1);
    stop2=1;


%777777777SCAN THE MATRIX
for i=1:24

    a = fscanf(ofile,'%f',1);
    b = fscanf(ofile,'%s',1);
    a = fscanf(ofile,'%f',1);
    a = fscanf(ofile,'%f',1);
    hf(25-i,it,irodi) = fscanf(ofile,'%f',1);
    a = fscanf(ofile,'%f',1);
    b = fscanf(ofile,'%s',1);
```

116

```matlab
        cot(25-i,it,irodi) = fscanf(ofile,'%f',1);
        b = fscanf(ofile,'%f',1);
        b = fscanf(ofile,'%f',1);
        b = fscanf(ofile,'%f',1);
        b = fscanf(ofile,'%f',1);
        b = fscanf(ofile,'%f',1);
        b = fscanf(ofile,'%f',1);
        fenth(25-i,it,irodi) = fscanf(ofile,'%f',1);

end
  %777777777


    end
    end
%$$$$$$$$$$$$$$$$$$$$$$$$$$$$$$$$$$$$$$$$$$$$$$$$$$


    end
    end
    end
end
%=================================================


end
end
end
end
end
end
end
end
end
%+++++++++++++++++++++++++++++++++++++++++++++++++++++


fclose(ofile);

end



for ichi=1:nchi
ichi
ofile = fopen('outptt','r');
it=0;


%+++++++++++++++++++++++++++++++++++++++++++++++++++++
while ~feof(ofile)

% search for Beginning of data
dum = fscanf(ofile,'%s',1);
```

```
if
(strcmp(dum,'iterative')||strcmp(dum,'direct')||strcmp(dum,'recirc'))
dum = fscanf(ofile,'%s',1);
if strcmp(dum,'solution')
dum = fscanf(ofile,'%s',1);
if strcmp(dum,'(idrect')
dum = fscanf(ofile,'%s',1);
if strcmp(dum,'=')
dum = fscanf(ofile,'%s',1);
if strcmp(dum,'2)')
dum = fscanf(ofile,'%s',1);
if strcmp(dum,'-')
dum = fscanf(ofile,'%s',1);
if strcmp(dum,'time')
dum = fscanf(ofile,'%s',1);
if strcmp(dum,'=')
it=it+1;
time(it) = fscanf(ofile,'%f',1);


%------------------------------------------------------------
% Search for the channel of interest
stop=0;
while stop==0
    dum = fscanf(ofile,'%s',1);
    if strcmp(dum,'channel')
    ch = fscanf(ofile,'%d',1);
    if ch==chofint(ichi)
        stop=1;

%      within the channel of interest, read the data
stop2=0;

%$$$$$$$$$$$$$$$$$$$$$$$$$$$$$$Search for beginning of matrix
while stop2==0
    dum = fscanf(ofile,'%s',1);
    if strcmp(dum,'(btu/sec-ft)')
    dum = fscanf(ofile,'%s',1);
    stop2=1;

%777777777SCAN THE MATRIX
for i=1:24

    a = fscanf(ofile,'%f',1);
    b = fscanf(ofile,'%s',1);
    a = fscanf(ofile,'%f',1);
    a = fscanf(ofile,'%f',1);
    m(25-i,it,ichi) = fscanf(ofile,'%f',1);
    b = fscanf(ofile,'%s',1);
    b = fscanf(ofile,'%f',1);
    b = fscanf(ofile,'%f',1);
    h(25-i,it,ichi) = fscanf(ofile,'%f',1);
    b = fscanf(ofile,'%f',1);
    b = fscanf(ofile,'%f',1);
```

```
    b = fscanf(ofile,'%f',1);
    b = fscanf(ofile,'%f',1);

end
  %777777777


    end
    end
%$$$$$$$$$$$$$$$$$$$$$$$$$$$$$$$$$$$$$$$$$$$$$$$$$$


    end
    end
end
%---------------------------------------------------------


end
end
end
end
end
end
end
end
end
%+++++++++++++++++++++++++++++++++++++++++++++++++++++


fclose(ofile);
end


cotc = (cot-32)*5/9; %Convert cladding outside temperature to degrees C


fclose(ofile);
```

10.6 Transient DNB routine

The routine for transient DNB, which calculates quasi steady-state DNB and the variation of the liquid layer thickness with time, is shown in Listing 10.17. The following external functions are used:

- Groeneveld(g,x,p) is a function providing the critical heat flux from the 2006 CHF look-up table (Groeneveld et al. 2007)

- XSteam is a function with water properties.

Listing 10.17, Transient CHF routine

```matlab
% variable | meaning
% ***************************
% chf          critical heat flux
% dnbr         DNBR
% mdnbr        MDNBR
% sschf_flag   flag for steady-state DNB
% delta        liquid layer thickness
% derHI        HI term - derivative of delta with time
% derTH        thermal thinning term - derivative of delta with time


ich=5;     %choose the channel and rod of interest
irod=5;


[nz,nt]=size(h);


pkPa = 15500; %pressure in kPa


h_f_british = 701; % in BTU/lbm from 1630 kJ/kg
h_g_british = 1117; % in BTU/lbm from 2596 kJ/kg


x = (squeeze(h(:,:,ich)) - h_f_british) ./ (h_g_british - h_f_british);
gSI = squeeze(m(:,:,ich)) * 1356;
hfSI = abs(squeeze(hf(:,:,irod)))*0.0031525*1000*1;
hSI = abs(squeeze(h(:,:,irod)))*2.325*1000;


[dum,ntimevip]=size(time);
chf = zeros(nz,ntimevip);


for it = 1:ntimevip
    for iz = 1:nz

        if (gSI(iz,it))<0
          gSI(iz,it)=0;
        end

        if (gSI(iz,it))>8000
          gSI(iz,it)=8000;
        end

% Critical heat flux according to the 2006 CHF look-up table
k1 = 0.7696;
k2(iz,it)=min(1,(0.5+2*0.393847)*exp(-0.5*nthroot(x(iz,it),3)));
chf(iz,it) = k2(iz,it)*1000*k1*Groeneveld(gSI(iz,it),x(iz,it),pkPa);


    end
end
```

```matlab
dnbr = chf./hfSI; % Calculate DNBR
mdnbr=min(dnbr);   % Minimum DNBR


pbar = 155;
h_g=XSteam('hV_p',pbar)*1000;
h_f=XSteam('hL_p',pbar)*1000;
h_fg=h_g-h_f;
rho_g=XSteam('rhoV_p',pbar);
rho_f=XSteam('rhoL_p',pbar);
sigma=XSteam('st_p',pbar);


f_1=(pi*sigma*((rho_f+rho_g)/(rho_f*rho_g))*...
        0.0584^2*(rho_g/rho_f)^0.4*(rho_g*h_fg)^2)/2;
f_11=-pi*sigma*h_fg^2*rho_g*(rho_f+rho_g)...
    *0.0584^2*(rho_g/rho_f)^0.4/rho_f;


sschf_flag=0; %if 0, no sschf, if 1 no trchf, if 2 trchf has occurred


derHI=zeros(1,ntimevip);
derTH=zeros(1,ntimevip);
delta=zeros(1,ntimevip);


%loop for calculating transient chf
for it = 1:ntimevip

    if sschf_flag==1 %do the calculation only if no sschf has yet
occurred
        dq_dt=(hfSI(zchfss,it)-hfSI(zchfss,it-1))/(time(it)-time(it-
1));
        h_lg=h_g-hSI(zchfss,it);

        derHI(it) = f_11*(dq_dt/hfSI(zchfss,it)^3);
        derTH(it) = 1/rho_f/(1-0.0584*(rho_g/rho_f)^0.2)*...
        (chf(zchfss,it)^3/hfSI(zchfss,it)^2/h_fg-hfSI(zchfss,it)/h_lg);

        delta(it)=delta(it-1)+min(derHI(it),derTH(it))*(time(it)-
time(it-1));

        if delta(it)<0
            sschf_flag=2;
        end

    end

    if sschf_flag==0 %check when dnb occurs first time and change flag
to 1
    delta(it)=NaN;
    if mdnbr(it)<1 %if ss dnb has occurred for the first time
    sschf_flag=1;
```

```
    [minchfss,zchfss]=min(chf(:,it));

    delta_0=(1/min(chf(:,it))^2)*f_1; %initial liquid film thickness
    delta(it)=delta_0;
    end
    end

end
```